

THE PAN-STARRS1 MEDIUM-DEEP SURVEY: THE ROLE OF GALAXY GROUP ENVIRONMENT IN THE STAR FORMATION RATE VERSUS STELLAR MASS RELATION AND QUIESCENT FRACTION OUT TO $z \sim 0.8$

LIHWAI LIN¹, HUNG-YU JIAN², SEBASTIEN FOUCAUD^{3,1}, PEDER NORBERG⁴, R. G. BOWER⁴, SHAUN COLE⁴,
 PABLO ARNALTE-MUR⁴, CHIN-WEI CHEN¹, JEAN COUPON^{1,5}, BAU-CHING HSIEH¹, SEBASTIEN HEINIS⁶,
 STEFANIE PHLEPS⁷, WEN-PING CHEN⁸, CHIEN-HSIU LEE^{9,7}, WILLIAM BURGETT¹⁰, K. C. CHAMBERS¹⁰, L. DENNEAU¹⁰,
 P. DRAPER⁴, H. FLEWELLING¹⁰, K. W. HODAPP¹⁰, M. E. HUBER¹⁰, N. KAISER¹⁰, R.-P. KUDRITZKI¹⁰,
 E. A. MAGNIER¹⁰, N. METCALFE⁴, PAUL A. PRICE¹¹, J. L. TONRY¹⁰, R. J. WAINSCOT¹⁰, AND C. WATERS¹⁰

¹ Institute of Astronomy & Astrophysics, Academia Sinica, Taipei 106, Taiwan, R.O.C.; lihwailin@asiaa.sinica.edu.tw

² Department of Physics, National Taiwan University, Taipei 106, Taiwan, R.O.C.

³ Department of Earth Sciences, National Taiwan Normal University, N°88, Tingzhou Road, Sec. 4, Taipei 11677, Taiwan, R.O.C.

⁴ Institute for Computational Cosmology, Department of Physics, Durham University, South Road, Durham DH1 3LE, UK

⁵ Department of Astronomy, University of Geneva, ch. d'Ecogia 16, CH-1290 Versoix, Switzerland

⁶ Department of Astronomy, University of Maryland, MD 20742, USA

⁷ Max-Planck-Institut für Extraterrestrische Physik, Giessenbachstraße, D-85748 Garching, Germany

⁸ Graduate Institute of Astronomy, National Central University, Chung-Li 32054, Taiwan, R.O.C.

⁹ University Observatory Munich, Scheinerstrasse 1, D-81679 Munich, Germany

¹⁰ Institute for Astronomy, University of Hawaii, 2680 Woodlawn Drive, Honolulu, HI 96822, USA

¹¹ Department of Astrophysical Sciences, Princeton University, Princeton, NJ 08544, USA

Received 2013 October 30; accepted 2013 December 17; published 2014 January 23

ABSTRACT

Using a large optically selected sample of field and group galaxies drawn from the Pan-STARRS1 Medium-Deep Survey (PS1/MDS), we present a detailed analysis of the specific star formation rate (SSFR)—stellar mass (M_*) relation, as well as the quiescent fraction versus M_* relation in different environments. While both the SSFR and the quiescent fraction depend strongly on stellar mass, the environment also plays an important role. Using this large galaxy sample, we confirm that the fraction of quiescent galaxies is strongly dependent on environment at a fixed stellar mass, but that the amplitude and the slope of the star-forming sequence is similar between the field and groups: in other words, the SSFR—density relation at a fixed stellar mass is primarily driven by the change in the star-forming and quiescent fractions between different environments rather than a global suppression in the star formation rate for the star-forming population. However, when we restrict our sample to the cluster-scale environments ($M > 10^{14} M_\odot$), we find a global reduction in the SSFR of the star-forming sequence of 17% at 4σ confidence as opposed to its field counterpart. After removing the stellar mass dependence of the quiescent fraction seen in field galaxies, the excess in the quiescent fraction due to the environment quenching in groups and clusters is found to increase with stellar mass, although deeper and larger data from the full PS1/MDS will be required to draw firm conclusions. We argue that these results are in favor of galaxy mergers to be the primary environment quenching mechanism operating in galaxy groups whereas strangulation is able to reproduce the observed trend in the environment quenching efficiency and stellar mass relation seen in clusters. Our results also suggest that the relative importance between mass quenching and environment quenching depends on stellar mass—the mass quenching plays a dominant role in producing quiescent galaxies for more massive galaxies, while less massive galaxies are quenched mostly through the environmental effect, with the transition mass around $1\text{--}2 \times 10^{10} M_\odot$ in the group/cluster environment.

Key words: galaxies: evolution – galaxies: groups: general – galaxies: high-redshift – large-scale structure of universe

Online-only material: color figures

1. INTRODUCTION

One of the most important findings related to galaxy formation and evolution in the last three decades is the well-known correlation between galaxy properties and their hosting environments, often referred as the star formation rate (hereafter SFR)—density, morphology—density, and color—density relations (Dressler 1980; Balogh et al. 1998; Gómez et al. 2003; Kauffmann et al. 2004; Gerke et al. 2007; Cooper et al. 2007; Elbaz et al. 2007). On average, galaxies tend to be more massive, redder, and less active in star formation in denser environments, such as galaxy groups and clusters. The main drivers for this relationship can be divided into two categories: the consequence

of an older population in massive halos due to the earlier formation of galactic halos in overdense regions that are destined to become galaxy clusters, the so-called nature process, versus nurture process, which refers to the physical mechanisms acting on the galaxies located in groups or clusters. In the “nature” processes, galaxies living in more massive halos are formed earlier and have accumulated more stellar masses compared to galaxies in the field. As a result, galaxies residing in denser environments show older stellar populations and their stellar mass (luminosity) function is shifted toward the more massive (luminous) end (Kauffmann et al. 2004; Baldry et al. 2006; Robotham et al. 2006; Muzzin et al. 2012). Examples of the “nurture” processes include ram-pressure stripping (Gunn & Gott 1972; Dressler

& Gunn 1983), high speed galaxy encounters (galaxy harassment; Moore et al. 1996), galaxy–galaxy mergers (Mihos & Hernquist 1994), and removal of warm and hot gas (strangulation; Larson et al. 1980; Balogh et al. 2000). Undoubtedly both the processes of nature and nurture are responsible for the observed SFR–density relation, however, the key question is which one plays a more important role in the evolution of galaxies.

One intriguing way to decipher the relative role between nature and nurture processes is to compare the SFR of galaxies for a given stellar mass (hereafter M_*). The nature process predicts that the main difference in galaxy properties in different environments is driven by the difference in their stellar mass distributions. In contrast, the nurture process alters the properties of galaxies of a given stellar mass. The star formation rate–stellar mass (SFR– M_*) relation therefore provides key insights into the physical processes that drive and regulate the star formation activities in galaxies as well as the stellar mass assembly histories of galaxies.

A tight correlation between galaxy SFR and M_* for star-forming (SF) galaxies (the so-called main sequence) has been observed for star-forming galaxies out to $z \sim 2$ (Brinchmann et al. 2004; Noeske et al. 2007; Elbaz et al. 2007; Daddi et al. 2007; Pannella et al. 2009; Magdis et al. 2010; Lin et al. 2012; Whitaker et al. 2012; Heinis et al. 2014). The normalization, slope, and scatter of this SFR– M_* relation carry a wealth information on the evolution of galaxies. For example, earlier works have found that the amplitude of this main sequence increases from $z \sim 0$ to $z \sim 2$, which can be understood as the global change of the gas density over time, being greater at higher redshifts. On the other hand, the slope of this relationship directly probes the SFR efficiency as a function of stellar mass: slope smaller than unity means that on average less massive galaxies form stars with greater efficiency. Finally, the scatter of the main sequence is found to remain approximately constant over this redshift range (Daddi et al. 2007; Whitaker et al. 2012), indicating that the physical processes leading to a smooth and steady supply of gas at higher redshifts are not that different from the ones which act at lower redshifts.

To better understand the role of environment in shaping galaxy properties, it is therefore intriguing to look into the environment dependence of the SFR– M_* relation, in addition to its redshift evolution. Recent studies using local samples have shown that the environment mostly changes the fraction of passive galaxies, resulting in the observed SFR–density relation, but has little effect on the SFR– M_* relation of the star-forming galaxies (Peng et al. 2010; Wijesinghe et al. 2012). This implies that the timescale of the quenching process occurring in dense environment must be relatively short so that galaxies move quickly from the star-forming sequence into the passive population, without changing the mean properties of the main-sequence. One favorable scenario responsible for environment quenching is attributed to the so-called satellite quenching: galaxies experience truncation of their star formation due to tidal stripping, ram-pressure stripping, and/or shock heating when they fall into bigger halos (McGee et al. 2011; Bolzonella et al. 2010; Wetzel 2011).

Extending this kind of study beyond local universe is challenging because of the difficulties in acquiring a large number of stellar mass selected samples with spectroscopic redshifts that are ideal for the environment measurement or identification. Several attempts have been made to push the study on the environment effect using group and cluster samples out to $z \sim 2$ (Patel et al. 2011; Vulcani et al. 2010; Muzzin et al. 2012;

Koyama et al. 2013; Alberts et al. 2014), but the conclusions are still controversial. Most recently, Koyama et al. (2013) compared the SFR– M_* relation for the H α -selected sample between field and clusters out to $z \sim 2.2$ and found that the SFR– M_* relation in clusters evolves in a similar manner as in the field since $z \sim 2$. However, their sample size is still small (one cluster per redshift bin), and they were not able to quantify the difference in the fraction of passive (quiescent) populations between different environments due to the H α -selection.

In this work, we take advantage of the large sample of galaxy groups and field galaxies from the early Pan-STARRS (short for the Panoramic Survey Telescope & Rapid Response System) Medium Deep Survey (MDS) to quantify the differences in galaxy properties between the field and group environments. More specifically, we study the SFR– M_* distribution as well as the quiescent fraction versus stellar mass relation as a function of environment and redshift in the redshift interval $0.2 < z < 0.8$. Our goal is to understand whether the SFR–density relation is purely due to the higher proportion of quiescent galaxies in groups, or whether it is driven by the suppression of star formation in galaxies of all stellar mass in the group environment. The large survey volume enclosed in this data also allows us to divide the groups sample into group and cluster environments so that one can gain better insights on how different physical structures affect the galaxy properties. To achieve our goals, we introduce a scheme to properly correct for the field contamination and incompleteness of the group members to uncover the underlying SFR and M_* distribution of group galaxies (see Section 3.1 and Appendix). Using this approach, we are allowed to construct the largest sample up-to-date for the study of the SFR– M_* relation in different environments at intermediate redshifts.

Our paper is structured as follows. In Section 2, we describe the data and methods of measuring redshift, SFR, M_* , and group identification used in this analysis. We present the main results in Section 3. Section 4 discusses the important implications for our results in understanding the evolution of galaxies. We present our conclusions in Section 5. Throughout this paper we adopt the following cosmology: $H_0 = 100 h \text{ km s}^{-1} \text{ Mpc}^{-1}$, $\Omega_m = 0.3$, and $\Omega_\Lambda = 0.7$. We adopt the Hubble constant $h = 0.7$ when calculating rest-frame magnitudes. We use a Salpeter IMF when deriving stellar masses and SFRs. All magnitudes are given in the AB system.

2. DATA, SAMPLE SELECTIONS, AND METHODS

2.1. Pan-STARRS Data

Pan-STARRS 1 (hereafter PS1) is a 1.8 m telescopes equipped with a CCD digital camera with 1.4 billion pixels and 3° field of view, located on the summit of Haleakala on Maui in the Hawaii Islands (Onaka et al. 2008; Kaiser et al. 2010). The Pan-STARRS1 observations are obtained through a set of five broadband filters, which we have designated as g_{P1} , r_{P1} , i_{P1} , z_{P1} , and y_{P1} . Under certain circumstances Pan-STARRS1 observations are obtained with a sixth, “wide” filter designated as w_{P1} that essentially spans g_{P1} , r_{P1} , and i_{P1} . Although the filter system for Pan-STARRS1 has much in common with that used in previous surveys, such as Sloan Digital Sky Survey (SDSS; Abazajian et al. 2009), there are important differences. The g_{P1} filter extends 20 nm redward of g_{SDSS} , paying the price of 5577 Å sky emission for greater sensitivity and lower systematics for photometric redshifts, and the z_{P1} filter is cut off at 930 nm, giving it a different response than the detector response defined

z_{SDSS} . SDSS has no corresponding y_{P1} filter. Further information on the passband shapes is described in Stubbs et al. (2010).

There are two major components of the PS1 survey which started observations in 2010: the 3π survey and the MDS. The largest portion of time is devoted to the 3π survey (K. Chambers et al., in preparation), which is scanning the entire sky north of declination -30° in five filters, $g_{\text{P1}}r_{\text{P1}}i_{\text{P1}}z_{\text{P1}}y_{\text{P1}}$ (Tonry et al. 2012), in six separate epochs spanning ~ 3.5 yr, each epoch consisting of a pair of exposures taken ~ 25 min apart. Each field center is visited by a total of 20 exposures per year in all filters. By stacking all these exposures, PS1 will provide a $30,000 \text{ deg}^2$ survey of the sky to a depth expected to be somewhat greater than that of the SDSS (York et al. 2000), especially at redder wavelengths. The survey is expected to be completed early in 2014 and publicly released to the world in 2015. More details on the characteristics of the 3π are described in Magnier et al. (2013) and Metcalfe et al. (2013).

This paper uses images and photometry from the Pan-STARRS1 Medium-Deep Field survey. The PS1 Medium Deep Fields (MD fields) consist of 10 spatially well-separated fields, each with 7 deg^2 . MD fields are observed repeatedly with $g_{\text{P1}}r_{\text{P1}}i_{\text{P1}}z_{\text{P1}}y_{\text{P1}}$ filters (Stubbs et al. 2010; Tonry et al. 2012), with the goal to reach $\{26.0, 26.0, 26.3, 25.6, 24.3\}$ in AB magnitude respectively for point sources after the 3.5 yr period of the PS1 mission finishes. Observations of the MD fields are taken each night, cycling through the various Pan-STARRS1 filters, during that portion of the year that the fields are accessible at less than 1.3 airmasses. A nightly observation in a given filter consists of eight dithered exposures, with a typical cadence as shown in Table 3 of Tonry et al. (2012).

Nightly stacks of PS1 data are produced by Image Processing Pipeline (IPP; Magnier 2006). The Pan-STARRS1 IPP system performed flatfielding on each of the individual images, using white light flatfield images from a dome screen, in combination with an illumination correction obtained by rastering sources across the field of view. Bad pixel masks were applied, and carried forward for use in the stacking stage. After determining an initial astrometric solution, the flat-fielded images were then warped onto the tangent plane of the sky, using a flux conserving algorithm. The plate scale for the warped images is $0.200 \text{ arcsec pixel}^{-1}$.

Using the “Astromatic” software,¹² SCAMP (Bertin 2006), SWarp (Bertin et al. 2002), and SExtractor (Bertin & Arnouts 1996), we produced our own version of deep stacks and associated catalogs based on all the nightly stacks generated by IPP between 2010 May and 2011 December. The zeropoint of the photometry is calibrated against the SDSS-DR7 catalog. In addition, all PS1 MD fields are covered in Canada–France–Hawaii Telescope (CFHT) MEGACAM u^* -band taken by Eugene Magnier et al. as part of the PS1 efforts. We have also downloaded the calibrated u^* -band images from the CADCArchive system and produced deep stacks and catalogs following a similar process as for the PS1 images. The final six-band master catalogs based on the i_{P1} -band detected objects are generated by running SExtractor in dual mode. Because the median seeing varies from $0''.8$ to $1''.1$ across different bands, the fluxes measured using a fixed size of aperture sample different fractions of lights of galaxies. Therefore we have chosen to use the *AUTO* magnitude of the i_{P1} band to be the total i_{P1} -band magnitude. The colors are defined as the difference in the *ISO* magnitude that are output from SExtractor using the isoarea defined by the i_{P1} band.

Empirically we find that this approach yields the best performance of photometric redshift. This work makes use of data taken in two of the PS1 MD fields, namely MD04 and MD07, which cover well-known multi-wavelength extra-galactic fields, COSMOS and Extended Groth Strip respectively. The choice of these two fields is primarily driven by the availability of large number of redshifts, robust redshift identification, and high sampling rate of the zCOSMOS (Lilly et al. 2007) and DEEP2 (Newman et al. 2013) spectroscopic redshift samples which are crucial for the purpose of calibrating our photometric redshifts (see Section 2.2) and our group-finder algorithm (see Section 2.4). In the current version of the MD07 catalog used in this work, we reach the depth of $\{25.63, 25.05, 24.95, 25.03, 24.46, 23.18\}$ for $\{u^*g_{\text{P1}}r_{\text{P1}}i_{\text{P1}}z_{\text{P1}}y_{\text{P1}}\}$ at 5σ using the $1''$ aperture in radius. The depth of MD04 is comparable to MD07, except for y_{P1} which is ~ 1 mag shallower. Details are given in a companion paper by S. Foucaud et al. (in preparation).

2.2. Photometric Redshifts

Photometric redshifts (hereafter photo- z , or sometimes z_{ph}) are computed by fitting the six optical bands including PS1 *grizy*-band and CFHT u^* photometry with the publicly available EAZY code¹³ (Brammer et al. 2008). The templates adopted in this work are taken from one of the template sets provided by another public photo- z software “LePhare” (Arnouts et al. 1999; Ilbert et al. 2006),¹⁴ called “CFHTLS-SED,” which includes 66 templates originally constructed by Ilbert et al. (2006) based on four observed galaxy spectra from Coleman et al. (1980) and two starburst galaxy spectra from Kinney et al. (1996) to optimize the photometric redshift results for the CFHTLS dataset. The details are described in Ilbert et al. (2006) and Coupon et al. (2009).

The computation of photo- z involves several steps. First we ran EAZY only for galaxies with secured spectroscopic redshifts to determine the systematic zeropoint offsets in each band by measuring the medians of the differences in the photometry between the data and the best-fit templates. Then we applied the derived zeropoint offsets back to the data and measured the photo- z for all galaxies. The derived systematic zeropoint offsets are often negligible in u^* (-0.01 mag), g_{P1} (0.00 mag), r_{P1} (-0.01 mag), and z_{P1} bands (0.00 mag), and are slightly larger in i_{P1} (-0.05 mag) and y_{P1} (-0.059 mag) bands. In order to reduce the catastrophic outliers due to the confusion between the Lyman and Balmer breaks in the absence of near-infrared data, we have adopted a prior on the redshift distribution for any given range of i -band magnitude using a mock galaxy catalog constructed based on a semi-analytical model described in Guo et al. (2010).

Two large spectroscopic redshift surveys, the DEEP2 (Newman et al. 2013) and zCOSMOS (Lilly et al. 2007) samples, are used to calibrate the zeropoints and to characterize our photo- z performances in MD07 and MD04 respectively. Figure 1 compares our photo- z results against the spectroscopic redshifts in these two MD fields. Following the definition adopted by Ilbert et al. (2006), we quantify the photo- z accuracy (hereafter $\sigma_{\Delta z/(1+z_s)}$) using the normalized median absolute deviation (NMAD Hoaglin et al. 1983), defined as $1.48 \times \text{median}(\Delta z/(1+z_s))$, where z_{ph} is the photo- z , z_s is the spectroscopic redshifts, and $\Delta z = z_{\text{ph}} - z_s$. The outlier rate (hereafter η) is

¹² <http://www.astromatic.net>

¹³ <http://www.astro.yale.edu/ezay/>

¹⁴ <http://www.cfht.hawaii.edu/~arnouts/lephare.html>

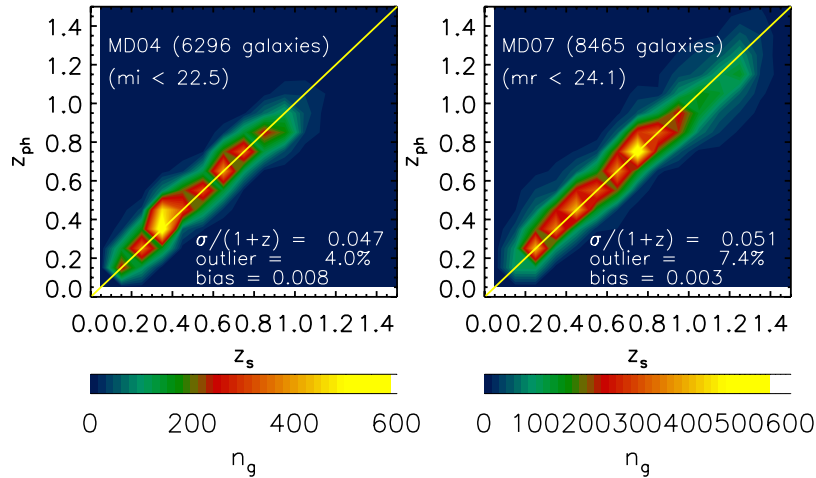


Figure 1. Photometric redshifts computed using PS1MD $g_{P1}r_{P1}i_{P1}z_{P1}y_{P1}$ and CFHT u^* filters vs. spectroscopic redshifts available in MD04 (left) and MD07 (right). The spectroscopic redshifts in MD04 are taken from the zCOSMOS 10 K sample (Lilly et al. 2007), and those in MD07 are drawn from the DEEP2 survey (Newman et al. 2013). Outliers are defined as objects with $\Delta z > 0.15 \times (1 + z_s)$.

(A color version of this figure is available in the online journal.)

defined as the fraction of galaxies with $\Delta z > 0.15 \times (1 + z_s)$. σ and η are found to be 0.047 and 4% at $i < 22.5$ in MD04, and 0.051 and 7% at $r < 24.1$ in MD07.

A complementary way of assessing the performance of the PS1 z_{ph} is to use overlapping photometric catalogues using a larger number of filters, thus providing more accurate values of z_{ph} . In this way, we can reproduce the same selection as in the PS1 catalogues, avoiding the possible biases introduced by the use of spectroscopic redshifts. We used the COSMOS v1.7 catalogue of Ilbert et al. (2009, 2010), which covers 2 deg^2 in field MD04, and contains photometric redshifts (z_{ph}^{cosmos}) computed with LePhare using 31 broad- and narrow-band filters. The error in the z_{ph}^{cosmos} ($\sigma \leq 0.011$ for $i^+ < 24$ and $z < 1.5$) is much smaller than that expected in PS1, so it is a good reference point for our comparison. For the limit used in this work, $i_{P1} < 24$, we found 93,733 objects which were present in the COSMOS catalogue. We define the dispersion (σ^P) and outlier rate (η^P) of the z_{phot} in this case in the same way as above, now taking $\Delta z = z_{ph} - z_{ph}^{\text{cosmos}}$, and obtain $\sigma^P = 0.083$ and $\eta^P = 20.8\%$ for the full catalogue. We also define the bias in the estimation of z_{ph} as the median of $\Delta z / (1 + z_{ph}^{\text{cosmos}})$, obtaining a value of bias = 0.014. We show the comparison between the PS1 and COSMOS redshifts in Figure 2. When restricting the comparison to objects with $i_{P1} < 22.5$ we found $\sigma^P = 0.050$, $\eta^P = 4.5\%$, bias = 0.012. We can use this comparison to characterize the redshift bins used in this work for galaxies with $i_{P1} < 24$. To this end, we introduce the bin outlier rate η_{bin} , defined as the fraction of objects selected in a given bin with a value of z_{ph}^{cosmos} farther than $1\sigma^P$ from the bin limits. For the first bin, $0.2 < z_{ph} < 0.5$, we found $\sigma^P = 0.065$, bias = 0.027 and $\eta_{bin} = 9.0\%$. For the bin in $0.5 < z_{ph} < 0.8$ we obtain $\sigma^P = 0.079$, bias = 0.022 and $\eta_{bin} = 23.5\%$.

As a further test, we made a comparison with the ‘‘Gold’’ catalogue of the ALHAMBRA survey (Molino et al. 2013), which provides z_{phot} down to $I < 23$ obtained using 23 bands (with an error $\sigma = 0.010$), and overlaps an area of $\sim 0.25 \text{ deg}^2$ in MD04 and $\sim 0.5 \text{ deg}^2$ in MD07. We found, for $i_{P1} < 22.5$, the values $\sigma^P = 0.048$, $\eta^P = 5.3\%$ and $\sigma^P = 0.047$, $\eta^P = 5.1\%$ for MD04 and MD07, respectively. We therefore conclude that the quality of our z_{phot} is consistent in the two fields considered. We restrict this study to the two MD catalogs (MD04 and MD07)

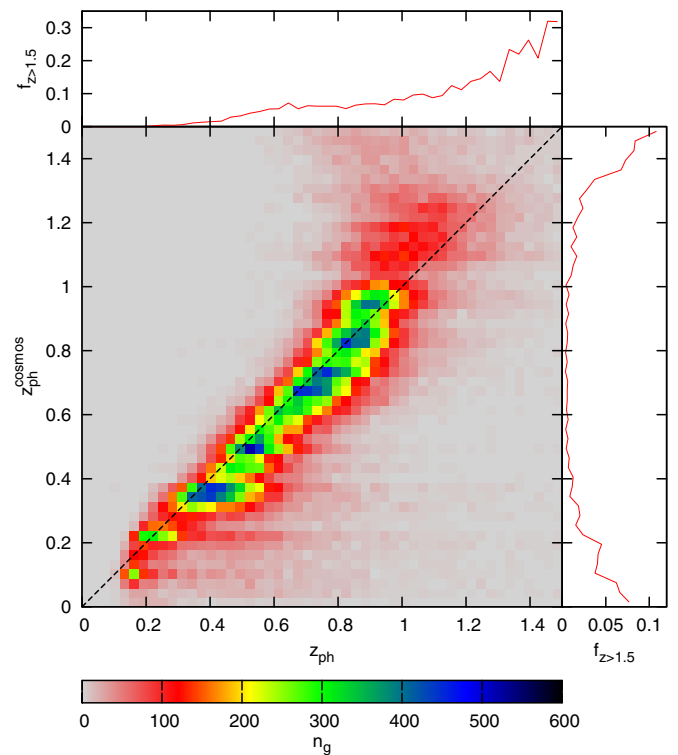


Figure 2. Photometric redshifts computed using the CFHT u^* and PS1MD $g_{P1}r_{P1}i_{P1}z_{P1}y_{P1}$ filters vs. the Ilbert et al. (2010) COSMOS photometric redshifts computed using 31 filters for the 100194 matched objects with $i_{P1} < 24$. The color map shows the number of galaxies (n_g) in bins of 0.03×0.03 . The top graph shows the fraction of objects with a given value of z_{ph} which have $z_{ph}^{\text{cosmos}} > 1.5$, and conversely the right-side graph shows the fraction of objects with a given value of z_{ph}^{cosmos} and $z_{ph} > 1.5$.

(A color version of this figure is available in the online journal.)

which consist of 313,997 galaxy-like objects brighter than $i_{P1} = 24$ mag over 14 deg^2 in the redshift between 0.2 and 0.8.

2.3. K-correction, Stellar Mass, and Star Formation Rate

The K-correction which converts the observed magnitudes to the rest-frame magnitudes is computed following a similar approach as described in Willmer et al. (2006). At a given redshift,

we fit a polynomial to the relationship between the K -correction term (using the observed bandpass closest to the desired rest-frame quantity) and a pair of adjacent observed color based on empirical templates taken from Kinney et al. (1996). Depending on the redshift, the corresponding polynomial formula is then applied to each galaxy in the redshift range of $0 < z < 1.45$.

We derive stellar masses by fitting the broad-band photometry to the synthesized templates generated with Bruzual & Charlot (2003) models using the spectral energy distribution (SED) fitting code “FAST” (Kriek et al. 2009). During the fitting, we fix the metallicity to be solar value¹⁵ and the redshift to be the photo- z determined from EAZY, while the rest of model properties including the age, star formation time scale τ (assuming an exponentially decaying star formation history), and dust content A_V are treated as free parameters.

For a subset of galaxies overlapped with the COSMOS field, we compared our derived stellar masses based on SED fitting to the six-band PS1 photometry to the ones in the COSMOS v1.7 photometric redshift catalog (Ilbert et al. 2010), computed with LePhare using the 31 broad- plus narrow-band COSMOS photometry data based on the same Bruzual & Charlot (2003) models. The COSMOS stellar masses were previously derived using the Chabier IMF, and hence we have multiplied those by a constant factor of 1.8 to convert them in to Salpeter IMF. In Figure 3 we show the comparison for galaxies (after correcting for the difference in the adopted IMF) whose PS1 z_{ph} are consistent with COSMOS z_{ph} within the typical PS1 photo- z uncertainty (i.e., $(z_{ph}^{ps1} - z_{ph}^{cosmos})/(1 + z_{ph}^{cosmos}) < 0.05$). We found that the scatter between the two measurements for “good” photometric redshift sample is ~ 0.23 dex.

To estimate the stellar mass completeness of our sample, we first translate the 5σ limiting magnitudes in the observed PS1 bands into the rest-frame quantities for galaxies at a given redshift, and then estimate the corresponding stellar mass using the empirical formula obtained by Lin et al. (2007) that relates the rest-frame magnitudes and colors to the stellar mass. For a fixed rest-frame magnitudes, the stellar mass is greater for galaxies with redder colors. Therefore we take the reddest colors of star-forming and quiescent populations respectively when computing the mass limit of the above two samples. This yields a mass limit $\log_{10}(M_*/M_\odot) = 9.4$ (9.0), 10.1 (9.7), and 10.5 (10.1) for red (blue) galaxies at $z \sim 0.2$, $z \sim 0.5$, and $z \sim 0.8$, respectively. The main sample used in this study contains 244,338 galaxies which have their stellar masses greater than $10^9 M_\odot$.

Unlike stellar masses, SFRs are rather sensitive to the degeneracies of the parameters in the SED fitting procedure in the case when there is not enough longer wavelength data. Instead of using the SFR output from FAST, we derived the SFR by adopting the approach described in Mostek et al. (2012) which parameterizes the SFR as a function of rest-frame optical U and B magnitudes (see Equation (1) and Table 3 in their paper) by calibrating against the [O II] emission line luminosities in the DEEP2 redshift sample (Newman et al. 2013). One caveat of this method is that it may be biased against highly dust-obscured populations (Mostek et al. 2012). However, as illustrated in Mostek et al. (2012), it uncovers the SFR of galaxies with a wide range of star formation activities, including both

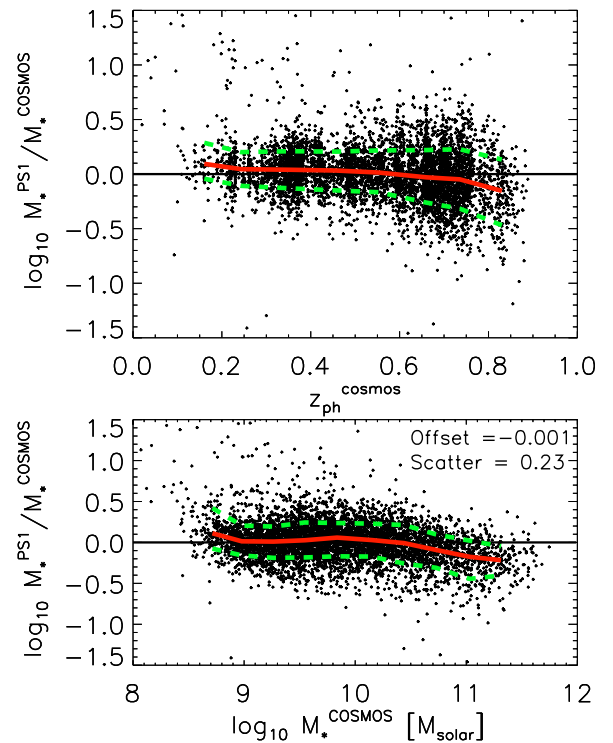


Figure 3. Difference in the stellar mass between our measurement and that from the COSMOS photo- z v1.7 catalog (Ilbert et al. 2010) after correcting for the difference in IMF, as a function of redshift (upper panel) and stellar mass (lower panel) for a matched sample in the COSMOS field (MD04). The black points are for all matched galaxies with whose PS1 photo- z agrees with the COSMOS photo- z (i.e., $(z_{ph}^{ps1} - z_{ph}^{cosmos})/(1 + z_{ph}^{cosmos}) < 0.05$). The red curve shows the median of the offset, while the lower and upper green curves represent the 16th and 84th percentiles, respectively. The scatter in this comparison is ~ 0.23 dex. (A color version of this figure is available in the online journal.)

blue and red galaxies and therefore is suitable for our purposes in a statistically representative way.

2.4. Group Identification

Proper identification of galaxy groups is essential to achieve our goals of studying galaxy properties in different environments. While spectroscopic redshift surveys have adequate redshift resolution to secure the group members, in practice it is observationally expensive to conduct a large-volume spectroscopic redshift survey with high sampling rate to yield statistically meaningful large numbers of groups of galaxies. Moreover, the spectroscopic sample has the tendency to be biased toward emission-line galaxies due to the greater signal-to-noise ratio in the line measurement for the redshift identification, which may possibly bias the results in particular for faint galaxies. In contrast, multi-band imaging surveys are relatively efficient at obtaining a large size of galaxy sample. However, group/cluster identification is challenging due to the lack of the redshift precision. One commonly adopted cluster identification method is the so-called red-sequence method which has proven to be successful in finding galaxy clusters by pinpointing the cluster redshifts (Gladders & Yee 2005). Nevertheless, this method relies on identifying the tight sequence in the red population and hence breaks down for group scales and suffers difficulty in recovering blue group members.

An alternative method, the Probability Friend-of-Friend group finder (hereafter PFOF; Liu et al. 2008), attempts to recover both the blue and red populations in groups. PFOF

¹⁵ To test the effect of metallicity, we compared the stellar masses derived with and without fixing the metallicity to be the solar value for a subsample with known spectroscopic redshifts, and found that the scatter between these two cases is ~ 0.1 dex.

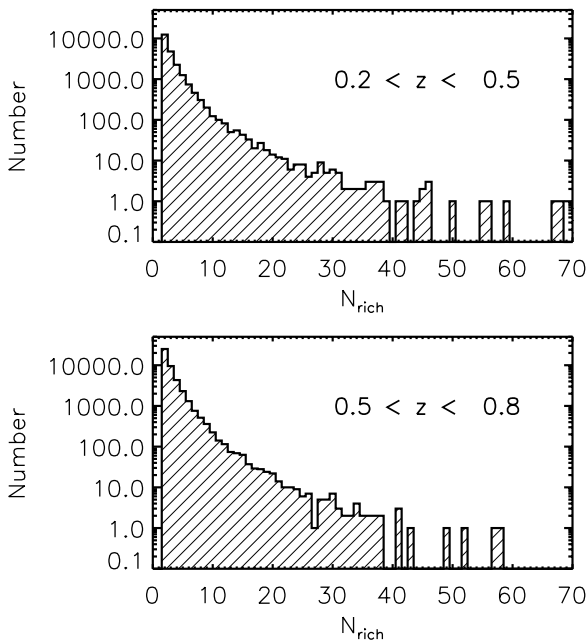


Figure 4. Richness (N_{rich}) distributions of the PFOF groups identified in MD04 and MD07. The distributions for the group samples in $0.2 < z < 0.5$ and $0.5 < z < 0.8$ are shown in the top and bottom panels, respectively.

considers the probability distribution function of photometric redshifts of each galaxy and computes the likelihood of a given pair of galaxies being spatially associated. The group sample is then constructed by linking galaxy pairs that have the likelihood exceeding a certain threshold, which is a free parameter determined in the process of optimizing the group memberships to the known spectroscopically identified groups and clusters in the same field.

The PFOF group finder has been tested intensively using galaxy mock catalogs as well as observational datasets (Liu et al. 2008; Jian et al. 2013). In Jian et al. (2013), we applied PFOF to the MD04 and MD07 photometric redshift catalogs, calibrated using the zCOSMOS and DEEP2 spectroscopically identified galaxy groups (Knobel et al. 2009; Gerke et al. 2012) respectively. The details are described in Jian et al. (2013). In this work, we make use of an updated version of the PFOF-generated group samples in MD04 and MD07 with the difference that instead of using different subset training samples in different fields, the two PFOF parameters, linking lengths in both the projected sky plane and the line-of-sight direction, and the probability threshold are trained by optimizing the purity and completeness against the DEEP2 spectroscopic identified group sample in the MD07. The same set of parameters are applied to both MD04 and MD07 as the photometric redshift uncertainty is comparable between the two fields.

Figure 4 shows the histogram of the richness (N_{rich}) for the 68,180 PFOF groups with $N_{\text{rich}} > 2$ identified in MD04 and MD07 in the redshift range of $0.2 < z < 0.8$, where N_{rich} is defined as the total number of members brighter than $i = 24$ in a group. In this work, we divide our PFOF group samples into two subsets, one with $10 < N_{\text{rich}} < 25$ (the “group” sample) and the other with $N_{\text{rich}} > 25$ (the “cluster” sample). For the group sample, the richness cut roughly translates into a group mass of $10^{13.2} < M_{\text{halo}} < 10^{13.8} M_{\odot}$ at $z \sim 0.4$ and $10^{13.4} < M_{\text{halo}} < 10^{14.0} M_{\odot}$ at $z \sim 0.8$ respectively. We consider field galaxies as those not associated with any groups with $N_{\text{rich}} \geq 2$. For any given group-finding method,

it is important to characterize its capability of recovering true group memberships as well as the contamination rate from the field galaxies. Jian et al. (2013) has shown that despite the photo- z uncertainty is in general worse for blue galaxies compared to that for red galaxies, with proper tuning of the linking length and the likelihood threshold, PFOF is able to recover blue members at a similar level as for red members. On the other hand, the contamination from blue galaxies in the field is typically larger than that from red galaxies. The reason for that is because the linking length cannot be too small otherwise we lose many blue members. Therefore the PFOF parameter optimization often leads to a linking length which is large enough to recover both blue and red galaxies at a similar level. The tradeoff is that the contamination rate from blue galaxies would become larger accordingly. This selection effect needs to be corrected when comparing the galaxy properties in different environments.

3. RESULTS

3.1. SFR- M_* Relation of Galaxies in Fields versus Groups

Figure 5 shows the SFR- M_* distribution for our sample of galaxies in the PS1 MD04 and MD07 fields, separated into bins of redshift: $0.2 < z < 0.5$ (upper panels) and $0.5 < z < 0.8$ (lower panels). The colors are scaled according to the numbers of galaxies enclosed in each SFR and M_* grid. The galaxies are further divided into “field” and “group” populations according to the PFOF identification (left-hand and middle panels). The stellar mass limits corresponding to galaxies at the upper- and lower- redshift limits, shown as vertical dashed lines, are computed using the method described in Section 2.3.

As mentioned in Section 2.4, the PFOF group catalogs are neither complete nor pure in terms of the memberships which may potentially bias our results when comparing the SFR- M_* distribution of galaxies in different environments. To characterize the selection function for star-forming and quiescent group members, we compute the recovery rate R_r and contamination rate R_c for star-forming and quiescent populations separately in bins of redshift and stellar mass, by cross-referencing the MD07 PFOF group catalogs to the spectroscopically identified group catalogs constructed in the EGS field (part of MD07) by Gerke et al. (2012). R_r is calculated as the fraction of spectroscopically identified group members that are also PFOF members, while R_c is computed as the fraction of PFOF group members that are not associated with spectroscopically identified groups. We provide more details in Appendix.

For each of the SFR and M_* grid, we then correct for both the incompleteness and contamination effects by subtracting the field contribution as follows:

$$n^g(\text{SFR}, M_*) = \frac{1 - R_c}{R_r} \times n_{\text{raw}}^g(\text{SFR}, M_*), \quad (1)$$

where $n^g(\text{SFR}, M_*)$ denotes the numbers of group galaxies for a given SFR and M_* grid. Ideally R_r and R_c should be computed in a SFR and M_* grid size as small as possible. However, our calibration relies on the limited numbers of spectroscopic group members, so we have chosen to compute R_r and R_c in six regions in the SFR and M_* space, and then for each region we apply the same global value to each SFR and M_* grid. The “corrected” group populations are shown in the right-hand panels of Figure 5.

In Figure 5, it can be seen that the distributions of field and group galaxies in the SFR and M_* plane are distinct. Qualitatively, the stellar masses of group galaxies are systematically

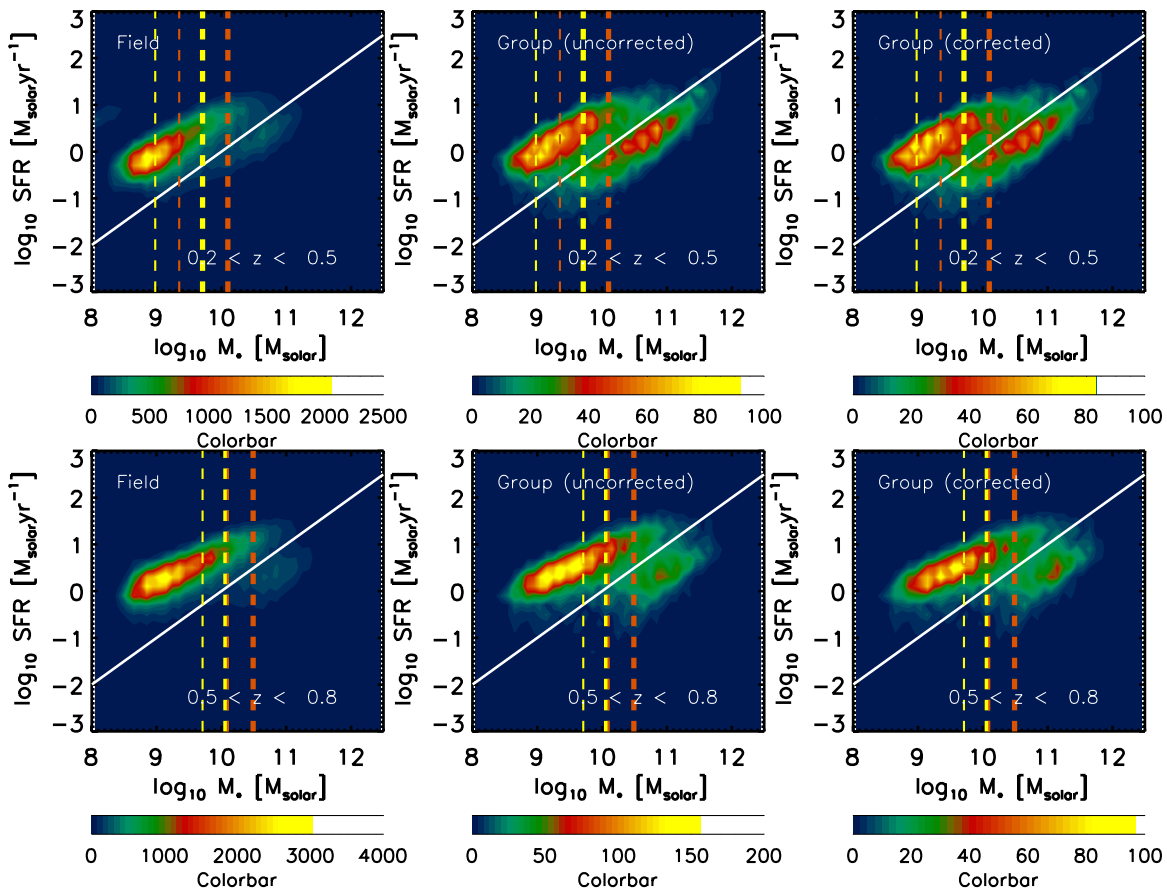


Figure 5. SFR and M_* distribution of galaxies in two of the PSIMD fields (MD04 and MD07), separated into bins of redshifts: $0.2 < z < 0.5$ (upper panels) and $0.5 < z < 0.8$ (lower panels). The colors are scaled according to the number of galaxies enclosed in each SFR and M_* grid. The left panels show results for field galaxies; the middle panels show results for galaxies identified in groups with masses in between 10^{13} and $10^{14} M_\odot$ by PFOF group-finding algorithm; the right panels give results for group galaxies after correcting for the completeness and contamination. The white solid line shows the dividing threshold ($SSFR = 10^{-10} \text{ yr}^{-1}$) separating the star-forming and quiescent population. The thick (thin) dashed lines represent the mass completeness limits for galaxies with the reddest colors in the star-forming (yellow lines) and quiescent (red lines) populations at the upper- (lower-) redshift limits of each panel.

(A color version of this figure is available in the online journal.)

shifted toward higher masses for both the star-forming and quiescent populations. In addition, the presence of the quiescent sequence is more prominent in the group environments, especially in the lower-redshift bin. This is in general in good agreement with previous studies concluding that the red fraction of galaxies is greater in the group than in the field (Gerke et al. 2007; Balogh et al. 2009; Giodini et al. 2012). For further analysis used in this work, we define star-forming and quiescent galaxies as those with specific star formation rate (SSFR) greater and lower than 10^{-10} yr^{-1} , respectively.

It is worth noting that in the high-redshift bin, there exists a class of massive star-forming galaxies with stellar mass $> 10^{10} M_\odot$ in the group which nevertheless is rare in the field environments in the similar redshift range. The presence of massive blue galaxies (or equivalently massive galaxies with high SFR) in dense environments at $z \sim 1$ has also been constantly reported in other studies (Gerke et al. 2007; Cooper et al. 2007; Tran et al. 2010; Koyama et al. 2013), suggesting a more advanced mass assembly stage in high-density regions. Our results suggest that while the fraction of quiescent galaxies in group environments is larger, galaxy groups, on average, are a preferential environment for the formation of massive star-forming galaxies.

To quantitatively describe the SFR– M_* relation of the main-sequence in our sample, we fit the data for the star-forming

Table 1
Best-fitting Parameters for the SFR– M_* Relation of the Star-forming Sequence in the Field and the Groups

Subsample	Number ^a	α	$\log_{10} \beta$
Field ($0.2 < z < 0.5$)	...	0.629 ± 0.007	-5.682 ± 0.068
Group ($0.2 < z < 0.5$)	610	0.638 ± 0.011	-5.813 ± 0.111
Cluster ($0.2 < z < 0.5$)	76	0.640 ± 0.026	-5.854 ± 0.264
Field ($0.5 < z < 0.8$)	...	0.591 ± 0.003	-5.170 ± 0.034
Group ($0.5 < z < 0.8$)	875	0.578 ± 0.012	-5.080 ± 0.119
Cluster ($0.5 < z < 0.8$)	61	0.602 ± 0.026	-5.370 ± 0.264

Note. ^a This column denotes the number of groups and clusters used in the analysis of each subsample.

galaxies with a linear relation between $\log_{10} \text{SFR}$ and $\log_{10} M_*$: $\log_{10} \text{SFR} = \alpha \times \log_{10} M_* + \log_{10} \beta$, where the slope α and the amplitude β are both fitting parameters. The best-fit results are given in Table 1. The best-fit slopes of the main sequence (star-forming population) in our field sample are between 0.59 and 0.63, in broad agreement with previous results at similar redshifts (Noeske et al. 2007; Whitaker et al. 2012), but slightly shallower compared to those found at $z \sim 2$ (Dunne et al. 2009; Pannella et al. 2009; Lin et al. 2012). The amplitude of the SFR– M_* relation in the lower- z bin is also in good agreement with the results from Noeske et al. (2007) who used the AEGIS

Table 2
The Mean SSFR and Quiescent Fraction in Different Environments

Subsample	Stellar Mass ($\log_{10}(M_{\odot})$)	SSFR ^{ALL} (yr^{-1})	SSFR ^{SF} (yr^{-1})	f_q
Field ($0.2 < z < 0.5$)	9.24	-9.23 ± 0.00	-9.17 ± 0.00	0.05 ± 0.00
	9.55	-9.35 ± 0.01	-9.23 ± 0.00	0.10 ± 0.00
	9.84	-9.51 ± 0.01	-9.31 ± 0.01	0.18 ± 0.01
	10.14	-9.73 ± 0.01	-9.43 ± 0.01	0.31 ± 0.01
	10.44	-10.00 ± 0.01	-9.57 ± 0.01	0.53 ± 0.02
	10.74	-10.20 ± 0.01	-9.71 ± 0.01	0.70 ± 0.02
	11.04	-10.30 ± 0.01	-9.71 ± 0.03	0.84 ± 0.04
	11.33	-10.23 ± 0.02	-9.74 ± 0.03	0.70 ± 0.05
Group ($0.2 < z < 0.5$)	9.25	-9.24 ± 0.01	-9.15 ± 0.01	0.08 ± 0.01
	9.55	-9.51 ± 0.02	-9.29 ± 0.01	0.21 ± 0.02
	9.85	-9.74 ± 0.02	-9.34 ± 0.02	0.36 ± 0.03
	10.15	-10.01 ± 0.02	-9.50 ± 0.02	0.52 ± 0.03
	10.45	-10.15 ± 0.02	-9.58 ± 0.02	0.70 ± 0.04
	10.73	-10.31 ± 0.01	-9.73 ± 0.02	0.83 ± 0.05
	11.05	-10.37 ± 0.02	-9.84 ± 0.02	0.87 ± 0.07
	11.34	-10.40 ± 0.03	-9.90 ± 0.02	0.93 ± 0.12
Cluster ($0.2 < z < 0.5$)	9.25	-9.38 ± 0.03	-9.22 ± 0.03	0.14 ± 0.03
	9.55	-9.62 ± 0.04	-9.31 ± 0.03	0.26 ± 0.04
	9.84	-9.90 ± 0.04	-9.38 ± 0.03	0.50 ± 0.06
	10.14	-10.12 ± 0.03	-9.47 ± 0.03	0.67 ± 0.06
	10.45	-10.24 ± 0.03	-9.64 ± 0.03	0.77 ± 0.08
	10.73	-10.29 ± 0.03	-9.74 ± 0.04	0.81 ± 0.09
	11.05	-10.36 ± 0.03	-9.70 ± 0.12	0.90 ± 0.13
	11.33	-10.42 ± 0.04	-9.95 ± 0.05	0.92 ± 0.20
Field ($0.5 < z < 0.8$)	9.25	-8.99 ± 0.00	-8.96 ± 0.00	0.02 ± 0.00
	9.55	-9.13 ± 0.00	-9.08 ± 0.00	0.03 ± 0.00
	9.84	-9.26 ± 0.00	-9.19 ± 0.00	0.05 ± 0.00
	10.14	-9.47 ± 0.01	-9.32 ± 0.00	0.13 ± 0.00
	10.44	-9.80 ± 0.01	-9.45 ± 0.00	0.33 ± 0.01
	10.74	-10.14 ± 0.01	-9.58 ± 0.01	0.56 ± 0.01
	11.04	-10.39 ± 0.01	-9.67 ± 0.01	0.77 ± 0.02
	11.34	-10.58 ± 0.01	-9.72 ± 0.02	0.89 ± 0.03
Group ($0.5 < z < 0.8$)	9.25	-9.02 ± 0.02	-8.96 ± 0.01	0.04 ± 0.01
	9.56	-9.15 ± 0.02	-9.09 ± 0.01	0.04 ± 0.01
	9.86	-9.33 ± 0.02	-9.22 ± 0.01	0.08 ± 0.01
	10.14	-9.60 ± 0.02	-9.39 ± 0.01	0.19 ± 0.02
	10.45	-9.91 ± 0.03	-9.51 ± 0.02	0.40 ± 0.03
	10.74	-10.18 ± 0.02	-9.61 ± 0.02	0.60 ± 0.04
	11.06	-10.44 ± 0.02	-9.70 ± 0.02	0.83 ± 0.06
	11.34	-10.57 ± 0.02	-9.74 ± 0.04	0.93 ± 0.08
Cluster ($0.5 < z < 0.8$)	9.24	-9.02 ± 0.04	-8.95 ± 0.03	0.05 ± 0.02
	9.55	-9.29 ± 0.05	-9.15 ± 0.03	0.10 ± 0.03
	9.86	-9.42 ± 0.05	-9.26 ± 0.03	0.13 ± 0.04
	10.15	-9.70 ± 0.05	-9.44 ± 0.03	0.26 ± 0.05
	10.45	-10.05 ± 0.06	-9.53 ± 0.03	0.49 ± 0.08
	10.75	-10.29 ± 0.05	-9.70 ± 0.03	0.64 ± 0.10
	11.06	-10.51 ± 0.04	-9.73 ± 0.05	0.89 ± 0.12
	11.34	-10.51 ± 0.05	-9.78 ± 0.06	0.87 ± 0.15

sample at $0.2 < z < 0.7$, after correcting for the difference in the IMF. From Table 1, we also see that both the slope and the amplitude between the field and group “main-sequence” are nearly the same, and the difference is only seen when the quenched population is included. We will discuss this further in the next section.

3.2. The SSFR– M_* Relation of Star-forming Galaxies

To have a closer view of the stellar mass dependence of the SFR, we measure the mean of SFR normalized by the stellar mass, namely, SSFR, in each stellar mass bin. These measurements are listed in Table 2. Galaxies are divided into the “star-forming” (SF) and “quiescent” (non-SF) populations

by their SSFR with a threshold of 10^{-10} yr^{-1} . Figure 6 shows the SSFR as a function of M_* for all galaxies (left panels) and for star-forming galaxies (right panels), separated according to their environments (field: purple symbols; groups: orange symbols). The error bars denote the standard errors (standard deviation divided by the square root of sample size in a given stellar mass bin), while the shaded areas show the dispersion of the SSFR at a given stellar mass. The slope of the SSFR– M_* relation becomes steeper when quiescent galaxies are included. While the difference in the median SSFR between field galaxies and group galaxies is apparent for the whole populations (left panels of Figure 6), it becomes more negligible when the quiescent galaxies are excluded (right panels of Figure 6). In other words,

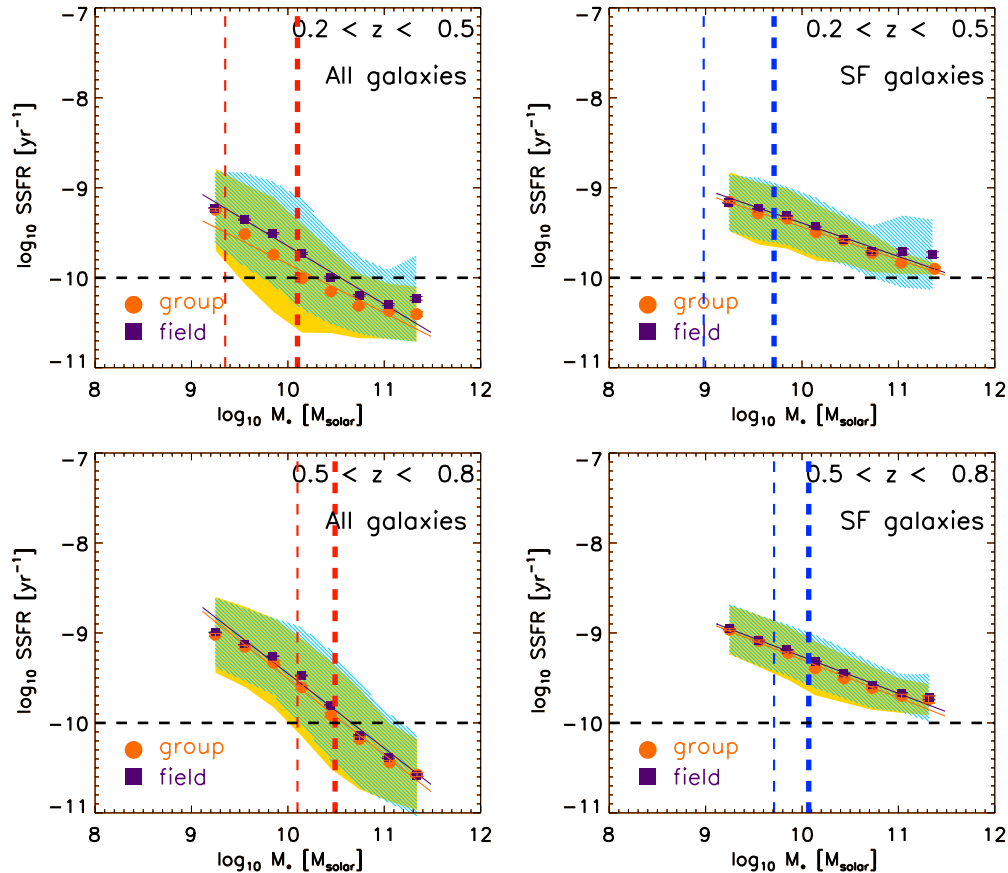


Figure 6. SSFR– M_* relation for all galaxies (two left panels) and for star-forming galaxies only (two right panels) in two redshift bins. The black horizontal dashed lines represent the SSFR threshold (10^{-10} yr^{-1}) that separates the “star-forming” (SF) and “quiescent” (non-SF) populations. Orange circles and purple squares show the means of the SSFR in each stellar mass bin for group and field galaxies respectively. The error bars denote standard errors (standard deviation divided by the square root of sample size in each bin). The shaded regions represent the 1σ standard deviation (yellow: groups; blue: field; green: the overlapped regions). The thick (thin) dashed lines represent the mass completeness limits for galaxies with the reddest colors in the star-forming (blue lines) and quiescent (red lines) populations at the upper- (lower-) redshift limits of each panel.

(A color version of this figure is available in the online journal.)

the group environment has little effect on the averaged star formation activities for “main-sequence” galaxies, whereas its effect is primarily on moving the galaxies out of the star-forming sequence toward the quiescent populations, leading to a suppressed of the mean SSFR of all (SF plus quiescent) group galaxies.

The difference in the SSFR– M_* relation for “all” galaxies between field and groups, however, becomes smaller with increasing redshift. This is consistent with the trend found in previous works that suggest a convergence of galaxy properties between field and groups at $z \sim 1$ by studying the colors and the red fractions of group galaxies as a function of redshift (Gerke et al. 2007).

3.3. The Stellar Mass and Environment Dependence of Quiescent Fraction and Quenching Efficiency

In the previous section, we have shown that for a given M_* the mean SSFR of group galaxies is lower compared to field galaxies only if quiescent galaxies are included in the analysis. We next turn to discuss how the fraction of quiescent galaxies depends on the stellar mass and environment (Table 2). Figure 7 displays the quiescent fraction f_q as a function of stellar mass in the field (purple symbols) versus groups (orange symbols). In both the redshift bins ($0.2 < z < 0.5$ and $0.5 < z < 0.8$), it can be seen that f_q increases rapidly with the stellar mass and this

trend is independent of environment, consistent with previous works (Quadri et al. 2012; Muzzin et al. 2012; Cheung et al. 2012; Kovac et al. 2013). In addition, f_q is in general higher in groups than in the field at fixed stellar mass.

To quantify the excess of quenching due to pure environment effects, it is useful to compute the so-called environment quenching efficiency by removing the stellar mass dependence. Assuming that the “mass quenching” and “environment quenching” are independent, the fraction of quenched galaxies in the group environments can be expressed as follows:

$$f_q^{\text{group}} = 1 - (1 - \epsilon^{\text{envi}}) * (1 - \epsilon^{\text{mass}}), \quad (2)$$

where ϵ^{envi} is the environment quenching efficiency, and ϵ^{mass} is the mass quenching efficiency. Assuming that only the mass quenching is in effect in the field environment, ϵ^{mass} is equivalent to f_q^{field} . Therefore, one can rewrite the environment quenching efficiency ϵ^{envi} as

$$\epsilon^{\text{envi}} = (f_q^{\text{group}} - f_q^{\text{field}}) / (1 - f_q^{\text{field}}). \quad (3)$$

As a result, ϵ^{envi} is identical to the fraction of galaxies that would be star-forming but which are however quenched in high-density regions as defined in Peng et al. (2010); Quadri et al. (2012).

Previous works have suggested that ϵ^{envi} has little dependence on stellar mass out to $z \sim 2$ (Peng et al. 2010; Quadri et al. 2012),

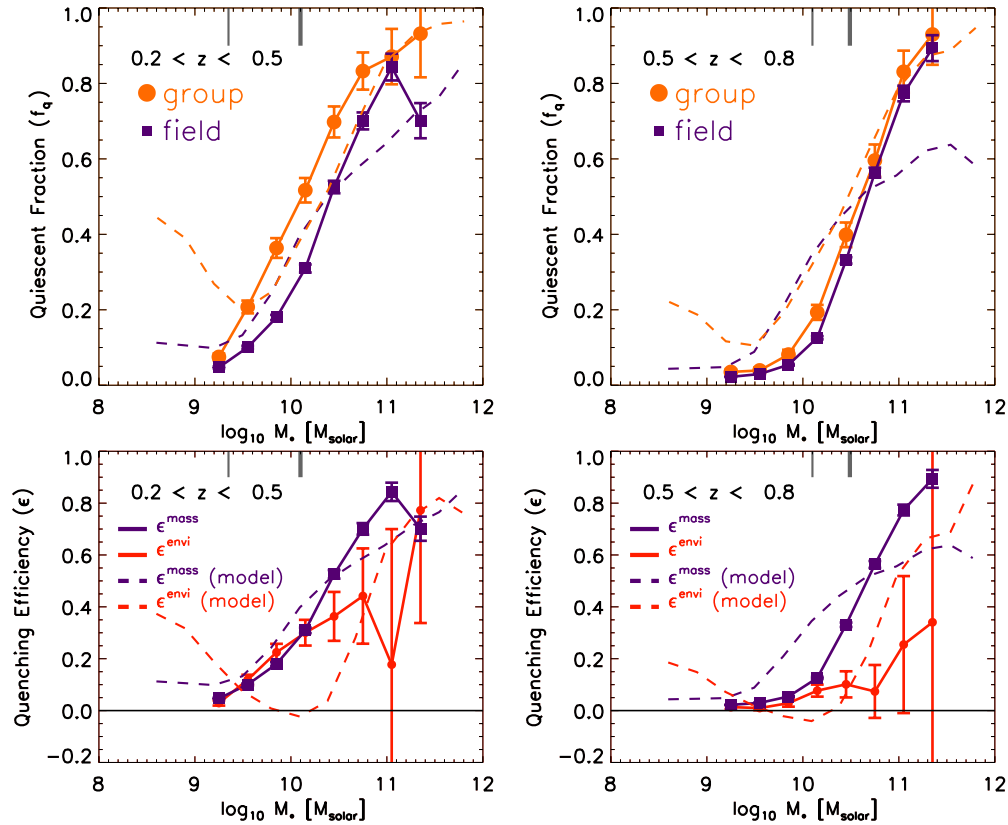


Figure 7. Upper panels: the fraction of quiescent population as a function of stellar mass in groups (orange symbols) and in the field (purple symbols). The purple and orange dashed curves show the theoretical predictions using the Font et al. (2008) model for galaxies located in the dark halos with masses of $10^{10} M_{\odot} < M_{\text{halo}} < 10^{12.5} M_{\odot}$ and $10^{12.5} M_{\odot} < M_{\text{halo}} < 10^{14} M_{\odot}$ respectively. Bottom panels: the environment quenching efficiency ϵ^{envi} (red curves) and mass quenching efficiency ϵ^{mass} (same as f_q^{field} ; purple curves) as a function of stellar mass. The gray thick (thin) ticks shown in the upper side of each panel denote the mass completeness limits for the reddest colors of galaxies at the upper- (lower-) redshift limit of each panel. The purple and red dashed curves show the stellar mass quenching and environment quenching efficiency predicted in the Font et al. (2008) model, respectively.

(A color version of this figure is available in the online journal.)

Table 3

The Mass Quenching Efficiency (ϵ^{mass}) and Environment Quenching Efficiency (ϵ^{envi}) in Groups and Clusters

Redshift	Stellar Mass ($\log_{10} (M_{\odot})$)	ϵ^{mass}	ϵ^{envi} (Group)	ϵ^{envi} (Cluster)
$0.2 < z < 0.5$	9.25	0.05 ± 0.00	0.03 ± 0.01	0.10 ± 0.03
	9.55	0.10 ± 0.00	0.12 ± 0.02	0.18 ± 0.04
	9.85	0.18 ± 0.01	0.22 ± 0.03	0.39 ± 0.07
	10.15	0.31 ± 0.01	0.30 ± 0.05	0.52 ± 0.10
	10.45	0.53 ± 0.02	0.36 ± 0.09	0.52 ± 0.16
	10.75	0.70 ± 0.02	0.44 ± 0.18	0.35 ± 0.30
	11.05	0.84 ± 0.04	0.18 ± 0.52	0.36 ± 0.87
$0.5 < z < 0.8$	11.35	0.70 ± 0.05	0.77 ± 0.43	0.73 ± 0.70
	9.25	0.02 ± 0.00	0.01 ± 0.01	0.03 ± 0.02
	9.55	0.03 ± 0.00	0.01 ± 0.01	0.07 ± 0.03
	9.85	0.05 ± 0.00	0.03 ± 0.01	0.09 ± 0.04
	10.15	0.13 ± 0.00	0.08 ± 0.02	0.15 ± 0.06
	10.45	0.33 ± 0.01	0.10 ± 0.05	0.24 ± 0.12
	10.75	0.56 ± 0.01	0.07 ± 0.10	0.18 ± 0.23
	11.05	0.77 ± 0.02	0.25 ± 0.26	0.51 ± 0.56
	11.35	0.89 ± 0.03	0.34 ± 0.83	-0.26 ± -1.49

meaning that the environment quenching acts at a similar level regardless of the stellar masses of galaxies. Nevertheless we note that the sample sizes used beyond the local universe were still very small. In the bottom panel of Figure 7, we plot ϵ^{envi} (red curves) as a function of stellar mass for the PS1MD sample (also see Table 3). In the redshift range we are probing, we find

a trend that ϵ^{envi} slightly increases with increasing stellar mass, different from the weak (or no) stellar mass dependence found in the zCOSMOS sample (Peng et al. 2010) and in the UKIDSS UDS sample (Quadri et al. 2012). We also find that the level of ϵ^{envi} becomes weaker in the higher-redshift bin, suggesting that the act of environment quenching operates more strongly in local universe than at higher redshifts at a fixed stellar mass.

3.4. Star-forming Sequence in Clusters

While the main focus of this work is to study the impact of the group environment on galaxies, we are also able to conduct a similar analysis for clusters that are found in MD04 and MD07 (see Table 2), thanks to the large cosmic volume probed by this catalog. In Figure 8, we again compare the SSFR- M_* relation against field galaxies but for 137 PFOF clusters selected with richness > 25 , roughly corresponding to $M_{\text{halo}} > 10^{14} M_{\odot}$. We found that the SSFR for star-forming galaxies with $M_* > 10^9 M_{\odot}$ in the clusters, in contrast to group galaxies, is lower than field star-forming galaxies by 17% with 4σ confidence. Furthermore, the environment quenching efficiency, is in general higher in the cluster case than in the group, as revealed in Figure 9 (see Figure 7 for the group results).

The higher quiescent fraction seen in the clusters compared to the field may be a result of the global reduction of the SSFR in the cluster galaxies, and/or proportionally more galaxies are being quenched in the groups. To examine the relative importance between the two effects, we also compute the fraction of galaxies

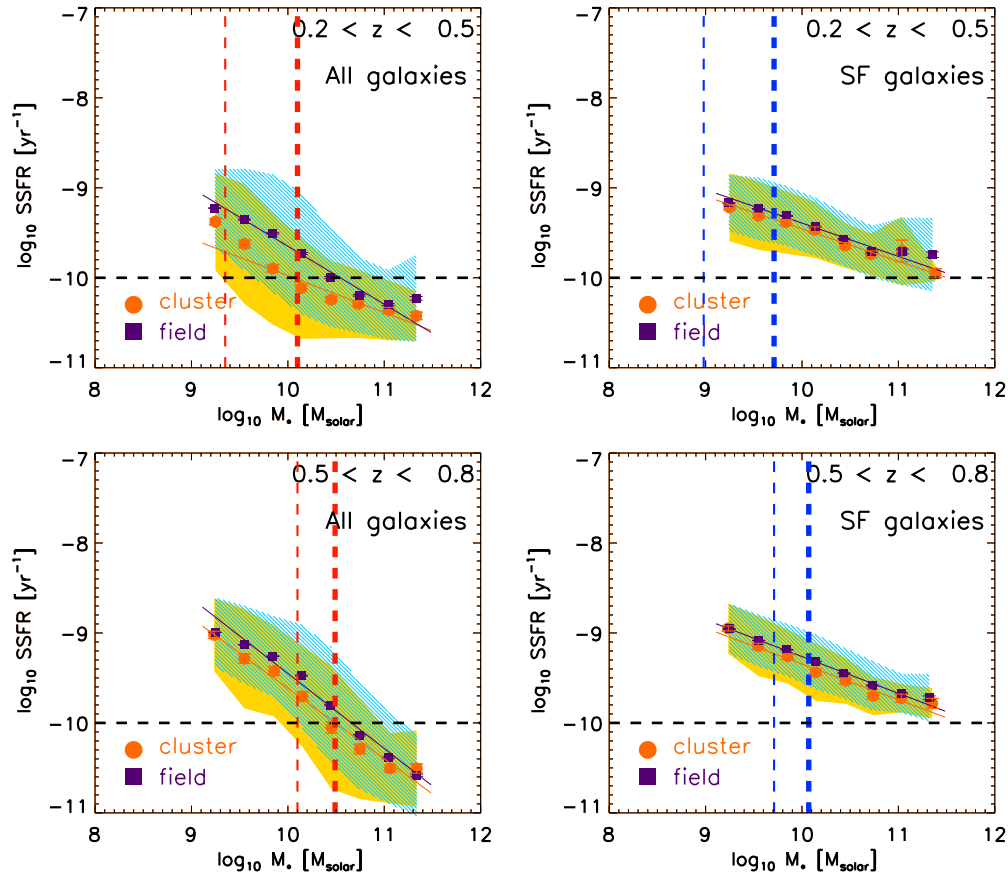


Figure 8. Similar to Figure 6 but for PFOF groups with $N_{\text{rich}} > 25$ (cluster-scale).

(A color version of this figure is available in the online journal.)

below the SSFR threshold value of 10^{-10} yr^{-1} in the case where the SSFR of field galaxies are lower by the amount of SSFR difference seen between the field and clusters. The results are shown in green colors in Figure 9. It reveals that the moderate reduction of the SSFR of the star-forming sequence alone cannot fully account for the excess of quiescent galaxies in the clusters. This implies that the influence of cluster environment may consist of both slow and fast quenching mechanisms: the former is responsible for the gradual suppression of the SFR, while the latter must happen in a timescale short enough to produce a notable difference in the quiescent fraction between the field and clusters. We will discuss this issue more in Section 4.

Now that we have shown that both the mass quenching efficiency ϵ^{mass} (or expressed as f_q^{field}) and the environment quenching efficiency ϵ^{envi} increase with the stellar mass, we proceed to compare the relative roles of these two effects as a function of stellar mass. The values of ϵ^{mass} and ϵ^{envi} are given in Table 3. In the bottom panel of Figures 7 and 9, we overplot ϵ^{mass} (same as the quantities f_q^{field} shown on the top panel). In the lower redshift bin ($0.2 < z < 0.5$), it is clear that the quenching process is dominated by the mass quenching for more massive galaxies whereas the environment is a secondary effect. However, the environment quenching exceeds the mass quenching for galaxies with stellar mass lower than a $1\text{--}2 \times 10^{10} M_\odot$. This transition mass increases slightly from the group to the cluster environments. In the higher redshift bin ($0.5 < z < 0.8$), there is also evidence that the mass quenching plays a more important role for massive galaxies,

but we cannot pinpoint the transition mass because the sample becomes incomplete below $3 \times 10^{10} M_\odot$.

4. DISCUSSION

Our results suggest that there are three effects contributing to the observed SFR–density relation: first, the quiescent fraction increases with the stellar mass; second, galaxies are progressively more massive in the group environment; and last, at a given stellar mass, the quiescent fraction is higher in the group environment than in the field. Furthermore, the effect of being in the group environment is primarily to increase the fraction of the quiescent population, rather than reducing the SFR of the entire population globally as the star formation activity of the star-forming galaxies in groups is not distinctly different from those in the field (Figure 6). Our main finding of this work is in good agreement with many previous studies (Balogh et al. 2004; Vulcani et al. 2010; Li et al. 2011; Wijesinghe et al. 2012; Koyama et al. 2013) and theoretical works (e.g., Cen 2013). However, our sample size is by far the largest among similar studies at the intermediate redshifts, and our sample includes both star-forming and passive populations that allow us to probe not only the properties of main-sequence galaxies but also the relative fraction between the star-forming and quiescent populations.

It has been long suggested that the bimodality of the galaxy colors (Blanton et al. 2003) implies a rapid star formation quenching process in moving galaxies from the blue cloud to the red sequence. The result that the SFR of star-forming sequence in the group environment is not globally reduced compared

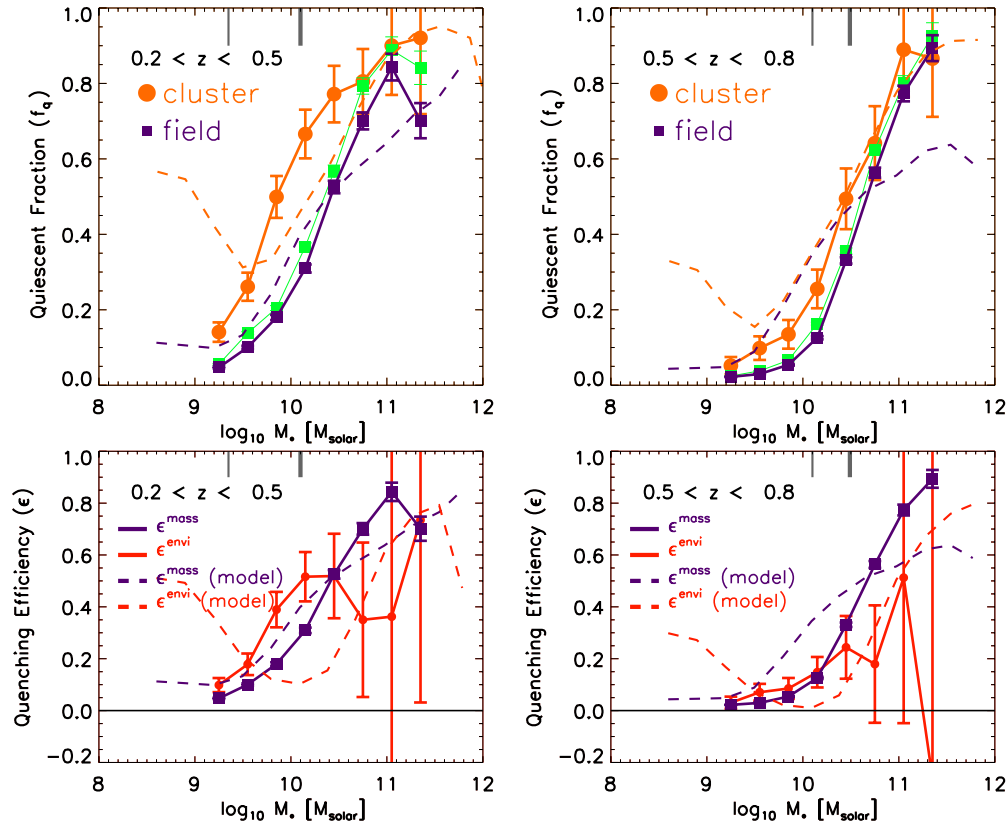


Figure 9. Similar to Figure 7 but for PFOF groups with $N_{\text{rich}} > 25$ (cluster-scale). The green data points present the quiescent fraction if the SFR of field galaxies is globally reduced by the amount of suppression seen in cluster SF galaxies (see text). The purple and orange curves show the theoretical predictions using the Font et al. (2008) model for galaxies located in the dark halos with masses of $10^{10} M_{\odot} < M_{\text{halo}} < 10^{12.5} M_{\odot}$ and $10^{14} M_{\odot} < M_{\text{halo}} < 10^{16} M_{\odot}$, respectively.

(A color version of this figure is available in the online journal.)

to their counterparts in the field suggests that the quenching mechanism operating in the groups/clusters is also a process during which the star formation is truncated in a very short period of time, leaving the SFR– M_* relation unaffected while increasing the quiescent population. In the absence of strong supernova feedback, this would favor the galaxy merger and ram-pressure stripping (of cold disk gas) scenarios which act on a short timescale < 1 Gyr (Gunn & Gott 1972; Lotz et al. 2010; Jian et al. 2012), over other mechanisms often invoked to explain the origin of the observed morphology–density or color–density relations found in clusters, such as strangulation, galaxy harassment, etc. However, ram-pressure stripping is thought to be more effective for clusters with mass $> 10^{14} M_{\odot}$ (Quilis et al. 2000; Bekki 2009). It is unlikely that it dominates the trend seen in our group sample, and therefore this leaves mergers as the most plausible process transforming galaxies from the star-forming sequence to the quiescent populations. Interestingly, earlier works based on the galaxy luminosity functions of blue and red galaxies in groups also infer that the changes in the galaxy properties in galaxy groups are consistent with the effects due to galaxy interactions (Robotham et al. 2006, 2010). Recent environment studies of galaxy mergers found that while most of the mergers occur in the intermediate environment which dominates the density distribution, the chance of galaxy mergers is actually higher in denser environments (Balogh et al. 2004; Lin et al. 2010; Kampczyk et al. 2013), peaked at the group environment (Jian et al. 2012). This provides another piece of evidence supporting the importance of mergers in high-density environments.

In the absence of strong feedback, all the above arguments lead to the conclusion that galaxy mergers are a favored process of environment quenching acting on group galaxies. Nevertheless, more recent theories of galaxy formation invoke very strong feedback to explain the low efficiency of star formation (Oppenheimer & Davé 2008; White & Frenk 1991; Balogh et al. 2004; Bower et al. 2006, 2012). In these models, galaxies receive gas flows into galaxies from the surrounding sheets and filaments at a high rate, but most of the incoming material is expelled by the galactic wind rather than formed into stars. When the galaxy becomes a satellite, this inflow is cut-off but the strong outflow continues to remove material from the galaxy. Because of the resulting imbalance between inflow and outflow, strangulation causes a rapid decline of the overall SFR in these models (Font et al. 2008). In these theories, strangulation also provides a viable explanation for the rapid transformation that is seen in the data (McGee et al. 2009; Wetzel et al. 2013).

When we compare the SFR and M_* distribution between field and cluster galaxies, we find that not only the quiescent fraction is significantly higher in the cluster environment, a moderate difference (17%) in the star formation activities between cluster and field SF galaxies for a fixed stellar mass is also detected. The suppression of the SFR of star-forming galaxies in clusters is possibly due to a longer timescale quenching process (e.g., strangulation and galaxy harassment). However, we cannot rule out the possibility that cluster members have been formed earlier and evolved over a longer period of time as opposed to field galaxies, and as a consequence have older stellar ages. Nevertheless, as shown in Figure 9, the amount of depleted

SSFR in clusters cannot account for the excess of the quiescent fraction relative to field, implying that a rapid quenching process is relatively more efficient than the mechanism that causes the suppression in the SSFR of star-forming cluster galaxies.

We can also compare our results with previous studies of cluster samples in a similar redshift range. Muzzin et al. (2012) has studied the SSFR– M_* relation and the star-forming fraction for a sample of nine clusters at $z \sim 1$ taken from the Gemini Cluster Astrophysics Spectroscopic Survey. They found that at a fixed stellar mass, the fraction of star-forming galaxies strongly correlates with the environment, but the SSFR– M_* relation is nearly identical between the field and clusters. A recent work by Koyama et al. (2013) investigated the star formation properties of $H\alpha$ -selected galaxies for three clusters at $z \sim 0.4, 0.8$, and 2.2 , respectively, and reached a similar conclusion that there is no notable difference in the SSFR– M_* relation between different environments. In contrast, Vulcani et al. (2010) detected a lower SSFR for star-forming members in clusters than their field counterparts by a factor of 1.5 based on 16 clusters at $0.4 < z < 0.8$ drawn from the Distant Cluster Survey (EDISCS). Most recently, Zeimann et al. (2013) also found that the SSFR of star-forming galaxies for a sample of 18 clusters at $1 < z < 1.5$ drawn from the IRAC Shallow Cluster Survey is systematically lower than the field galaxies at a fixed stellar mass. The discrepancy between these results is possibly due to the small size of the cluster samples utilized in their analysis. As revealed from our studies, the difference in the SSFR at a fixed stellar mass between the field and cluster galaxies is only moderate (17%), and therefore it is likely that the degree of SSFR suppression is under- or overestimated in previous studies due to the small number statistics.

Next we turn into the discussion of other implications of the similarity in the SFR– M_* relation between different environments. The star formation activity is believed to be regulated by the fueling of fresh gas and the feedback processes. Several galaxy formation models have shown that the SFRs are strongly related to the gas accretion rates, and the tightness of the SFR– M_* relation is a natural outcome of the relatively smooth and steady gas accretion of halos (Bower et al. 2006; Davé 2008; Dutton et al. 2010). In these models, the characteristics of the SFR– M_* relation is insensitive to the details in the feedback models, but governed by the rate of gas accretion, and hence by the rate of halo growth. If it is indeed true that there is a strong relationship between the SFR and the cold-gas accretion rate, one might naively expect that the SFR can differ in different environments as the gas accretion properties are dependent on the location of the cosmic web and on the halo mass. This leads to a puzzle as to why, in contrast to the simple expectation, the observed SFR is at a similar level for star-forming group galaxies as it is for field counterparts selected at the same stellar mass. A possible explanation is that the star-forming galaxies have only recently entered the group environment and are still embedded in distinct filaments or sub-halos that maintain the supply of gas onto the central galaxy. However, in order to make this viable the delay during which the gas supply is maintained must be long compared to the orbital time and must scale with redshift (McGee et al. 2009; Wetzel et al. 2013; Mok et al. 2013).

One of the interesting results from this work is the suggestion that the environment quenching efficiency is stronger for more massive galaxies. This is in contradiction to a naive expectation that smaller galaxies are more vulnerable to effects that remove gas supplies, such as tidal disruption or ram-pressure stripping, and therefore have a stronger SFR suppression or quenching

effect. Such a trend might result if more massive objects tend to be accreted on more radial objects, or experience more dramatic angular momentum loss due to dynamical friction, so that the halos of these objects experience greater ram pressure. Alternatively, it may simply arise from the biases in halo formation histories, with more massive galaxies being more likely to have been “pre-processed” in smaller groups prior to their accretion. On the other hand, there is also evidence showing that the galaxy merger rate increases with galaxy luminosity (and hence stellar mass) (Patton & Atfield 2008), which might be able to explain the increased quenching efficiency with increasing stellar mass in the groups. Nevertheless, it is worth noting that the mass limit of our sample is still constrained by the current MD depth. To push the analysis down to smaller mass range for more robust conclusions have to await till the completion of the full PS1/MD surveys.

Interestingly the mass-dependent environment quenching is also apparent in the strangulation model introduced by Font et al. (2008). By comparing the passive fractions in different bins of halo mass, we computed the environment quenching efficiency in the model in the same way we did for the observed data (i.e., using Equation (3)). The results are shown as a function of stellar mass in Figures 7 and 9. It is evident that ϵ^{envi} increases with stellar mass in this model, similarly to the observed trend. We emphasize that this stellar mass dependence of the environment quenching efficiency is not built in by hand but is rather a consequence of the Font et al. model. Therefore this provides a further support of the strangulation process adopted in Font et al. (2008) being a plausible mechanism that is responsible for the environment quenching in particular in the clusters.

Whether or not deeper data substantiate the suggestion that the impact of environment is greater for more massive galaxies, the relative importance of the environment with respect to mass quenching declines with the stellar mass as revealed in Figures 7 and 9, in good agreement with previous results from Alberts et al. 2014. The transition mass in which the quenching in central galaxies dominates is at roughly $1\text{--}2 \times 10^{10} M_\odot$, in good agreement with previous work (Kauffmann et al. 2003; Peng et al. 2010). Our results that the environment quenching is more important for small galaxies may shed light on the cosmic evolution of the galaxy number densities. For example, previous works have found that the number density of red galaxies has increased by at least a factor of two since $z \sim 1$ while the number density of blue galaxies has remained roughly constant (Bell et al. 2004; Faber et al. 2007). Using a stellar mass-selected sample drawn from the PRIMUS survey (Coil et al. 2011), Moustakas et al. (2013) further found that the increase in the number density of red galaxies is more prominent for low-mass galaxies. Qualitatively at least, this is consistent with the growth of large-scale structure. As the large-scale structure builds up, the number of galaxies belonging to the group and/or cluster environments increases with time. As a result, the number of low-mass galaxies being quenched through the environment effect also increases toward lower redshift, leading to the buildup of the red sequence over cosmic time. The challenge of course, is to reproduce the quantitative details of this behavior in cosmological models.

5. CONCLUSION

We have carried out an analysis of the SFR– M_* relation between field and group galaxies to study the environmental effect on shaping galaxy properties out to $z \sim 0.8$ using data

from the early PS1 MDS. Galaxy groups are identified using the group-finder PFOF (Jian et al. 2013) that is optimized for the PS1 photometric redshift sample. Galaxies are divided into the “star-forming” (SF) and “quiescent” (non-SF) populations by their SSFR with a threshold of 10^{-10} yr^{-1} . We study the $\text{SFR}-M_*$ relation with and without the inclusion of quiescent populations, and the quiescent fraction as a function of stellar mass in different environments. And finally we investigate the stellar mass dependence of the environment quenching efficiency.

Our main conclusions are as follows:

1. Group galaxies are found to be systematically more massive than galaxies in the field for both star-forming and quiescent populations, supporting the hierarchical scenario that galaxies are formed earlier in denser environments. In this picture, the existence of massive star-forming group galaxies in the higher-redshift bin ($0.5 < z < 0.8$) is a consequence of an earlier and faster evolution in group environment.
2. The normalization and slope of the $\text{SSFR}-M_*$ relation for star-forming galaxies are comparable between the field and group environments. On the other hand, the normalization is different when the quiescent galaxies are included in the analysis, being reduced for group galaxies.
3. Over the redshift range $0.2 < z < 0.8$, we find that the quiescent fraction is a strong function of the stellar mass, and is greater in the groups than in the field. The $\text{SFR}-\text{density}$ relation is the combination of these two effects plus the result from point 1 above. The excess of the quiescent fraction in the groups is responsible for the difference of the $\text{SFR}-M_*$ relation (all galaxies included) seen between field and groups.
4. The lack of the SFR suppression for star-forming galaxies and the higher quiescent fraction in groups suggest a fast quenching mechanism acting in the group environment. Galaxies, if being quenched, must have been moved from the star-forming sequence to the quiescent population in a relatively short time-scale to preserve the $\text{SFR}-M_*$ relation of the main-sequence. This favors galaxy mergers as a primary process that quenches the star-formation activities in galaxy groups, as other mechanisms are either inefficient at group scales (e.g., ram-pressure stripping) or operate over a longer time-scale (e.g., strangulation, and galaxy harassment, etc.) in the absence of strong feedback.
5. In contrast to the group environment, clusters have a more prominent effect on reducing the SSFR of the star-forming sequence. For a given stellar mass, the SFR is moderately lower by 17% at the 4σ confidence level in clusters than its field counterpart. Moreover, the quiescent fraction for clusters is found to be greater than that in both the group and field environments, leading to a greater environment quenching efficiency. The amount of the reduction in the SSFR of star-forming galaxies in clusters cannot fully account for the difference in the quiescent fraction between clusters and the field, however. This implies that the quenching mechanisms acting on the clusters involve both fast and slow processes.
6. In both the field and group environments, the quiescent fraction is a steep function of the stellar mass, being higher in more massive systems. Our results also indicate that the environment quenching efficiency increases with stellar mass, albeit a large sample is needed to draw a firm conclusion. A similar trend is also visible in the Font et al. (2008) model. At the cluster scale, this can be attributed

to the fact that massive galaxies are subject to stronger dynamical friction and shrink into the central part of clusters in a shorter timescale where the effect of tidal disruption and the ram-pressure is strongest. In groups, it is likely due to the increased galaxy merger frequency with increasing stellar mass.

7. The relative importance between mass quenching and environment quenching depends on the stellar mass of galaxies. In the lower redshift bin ($0.2 < z < 0.5$), the mass quenching plays a dominant role in producing quiescent galaxies for more massive galaxies, while less massive galaxies are quenched mostly through the environmental effect. This transition mass is around $1-2 \times 10^{10} M_\odot$ in group and cluster environments.

We thank the anonymous referee for constructive suggestions that further improve this paper. We also thank M. Kriek for releasing her SED fitting code “FAST,” and O. Ilbert and the COSMOS team for the usage of the stellar mass measurement from the unpublic V1.7 photometric redshift catalog. L.L. thanks F. Van de Voort, J. Heasley, and Y.-T. Lin for very helpful discussions, J.-K. Guo for helping with the PS1 data downloading and management, and N. Mostek for advising how their methods of estimating SFR can be used. We also thank PS1 staff who have provided help with the PS1 data observation and reduction. The work is supported by the National Science Council of Taiwan under grants NSC99-2112-M-001-003-MY3 and NSC 101-2112-M-001-011-MY2. H.-Y.J. acknowledges the support of NSC101-2811-M-002-075. W.-P.C. acknowledges the support of NSC 102-2119-M-008-001. P.N. acknowledges the support of the Royal Society through the award of a University Research Fellowship and the European Research Council, through receipt of a Starting Grant (DEGAS-259586). P.A.-M. and P.D. acknowledge support from a European Research Council Starting Grant (DEGAS-259586). Durham University coauthors were also supported by STFC, through grants ST/F001166/1 and ST/I001573/1, and by an ERC advanced grant (GA-267291). The Pan-STARRS1 Surveys (PS1) have been made possible through contributions of the Institute for Astronomy, the University of Hawaii, the Pan-STARRS Project Office, the Max-Planck Society and its participating institutes, the Max Planck Institute for Astronomy, Heidelberg and the Max Planck Institute for Extraterrestrial Physics, Garching, The Johns Hopkins University, Durham University, the University of Edinburgh, Queen’s University Belfast, the Harvard-Smithsonian Center for Astrophysics, the Las Cumbres Observatory Global Telescope Network Incorporated, the National Central University of Taiwan, the Space Telescope Science Institute, the National Aeronautics and Space Administration under grant No. NNX08AR22G issued through the Planetary Science Division of the NASA Science Mission Directorate, the National Science Foundation under grant No. AST-1238877, the University of Maryland, and Eotvos Lorand University (ELTE). PS1 images and catalogs will be made available through a Pan-STARRS PS1 data release by STScI. We close with thanks to the Hawaiian people for the use of their sacred mountain.

APPENDIX

FIELD CONTAMINATION AND GROUP COMPLETENESS CORRECTIONS

In this section, we describe the method we use to compute the field contamination rate R_c and the group member recovery rate

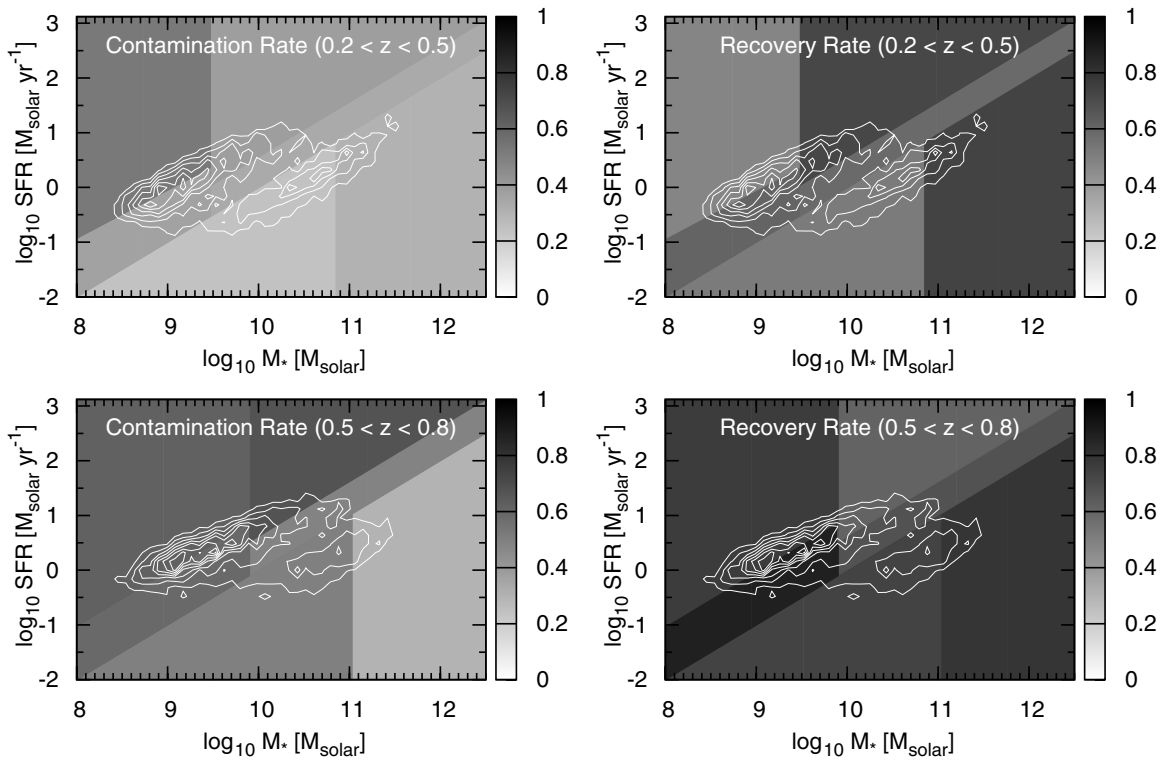


Figure 10. Correction factors for PFOF-identified groups. The field contamination rate R_c (left panels) and the group member recovery rate R_r (right panels) are shown in the background. The white contours show the density distribution of PFOF group galaxies.

R_r that are used to account for the contamination and incompleteness effects introduced in the PFOF group identification. We first cross match the MD07 photometric redshift catalog with the DEEP2 EGS spectroscopic galaxy sample (Newman et al. 2013). We then define a subset of the sample which only contains galaxies with secure spectroscopic redshift measurements. For each galaxy in this subsample, we have two flags indicating whether they are group members based on (1) MD PFOF's identification used in this work and (2) the DEEP2 group identification by Gerke et al. (2012). R_r is then calculated as the fraction of DEEP2 spectroscopically identified group members that are also PFOF members, while R_c is computed as the fraction of PFOF group members that are not associated with spectroscopically identified groups.

Since we are interested in the properties of galaxies on the SFR and M_* plane, ideally the two quantities R_c and R_r should be computed on a fine grid of SFR and M_* . However, the correction scheme we adopt relies on the spectroscopic sample whose sample size is not large enough for this purpose. We instead divide the galaxies into six sub-regions on the SFR and M_* plane when computing R_c and R_r . SF galaxies are grouped into four main regions: above and below the main sequence, for both large and small galaxies; while the quiescent galaxies are divided into large and small galaxies. For galaxies that are less massive than the mass limit of the spectroscopic redshift sample due to the difference in the depth and filter cut between the two surveys ($R < 24.1$ for the EGS versus $i_{p1} < 24$ for the PS1 MD), we adopt the same values of R_c and R_r as those derived in the smallest mass bins. The resulting R_c and R_r are shown in Figure 10. To test the robustness of our correction factors, we have also tested our results by varying the number of sub-regions and the choice of the dividing lines, and found that none of our conclusions presented in this work is significantly changed.

REFERENCES

- Abazajian, K. N., Adelman-McCarthy, J. K., Agüeros, M. A., et al. (The SDSS Collaboration) 2009, *ApJS*, **182**, 543
- Alberts, S., Pope, A., Brodwin, M., et al. 2014, *MNRAS*, **437**, 437
- Arnouts, S., Cristiani, S., Moscardini, L., et al. 1999, *MNRAS*, **310**, 540
- Baldry, I. K., Balogh, M. L., Bower, R. G., et al. 2006, *MNRAS*, **373**, 469
- Balogh, M., Eke, V., Miller, C., et al. 2004, *MNRAS*, **348**, 1355
- Balogh, M. L., McGee, S. L., Wilman, D., et al. 2009, *MNRAS*, **398**, 754
- Balogh, M. L., Navarro, J. F., & Morris, S. L. 2000, *ApJ*, **540**, 113
- Balogh, M. L., Schade, D., Morris, S. L., et al. 1998, *ApJL*, **504**, L75
- Bekki, K. 2009, *MNRAS*, **399**, 2221
- Bell, E. F., Wolf, C., Meisenheimer, K., et al. 2004, *ApJ*, **608**, 752
- Bertin, E. 2006, in ASP Conf. Ser. 351, *Astronomical Data Analysis Software and Systems XV*, ed. C. Gabriel, C. Arviset, D. Ponz, & E. Solano (San Francisco, CA: ASP), **112**
- Bertin, E., & Arnouts, S. 1996, *A&AS*, **117**, 393
- Bertin, E., Mellier, Y., Radovich, M., et al. 2002, in ASP Conf. Proc. 281, *Astronomical Data Analysis Software and Systems XI*, ed. D. A. Bohlender, D. Durand, & T. H. Handley (San Francisco, CA: ASP), **228**
- Blanton, M. R., Hogg, D. W., Bahcall, N. A., et al. 2003, *ApJ*, **594**, 186
- Bolzonella, M., Kovač, K., Pozzetti, L., et al. 2010, *A&A*, **524**, A76
- Bower, R. G., Benson, A. J., & Crain, R. A. 2012, *MNRAS*, **422**, 2816
- Bower, R. G., Benson, A. J., Malbon, R., et al. 2006, *MNRAS*, **370**, 645
- Brammer, G. B., van Dokkum, P. G., & Coppi, P. 2008, *ApJ*, **686**, 1503
- Brinchmann, J., Charlot, S., White, S. D. M., et al. 2004, *MNRAS*, **351**, 1151
- Bruzual, G., & Charlot, S. 2003, *MNRAS*, **344**, 1000
- Cen, R. 2013, *ApJ*, in press (arXiv:1311.5916)
- Cheung, E., Faber, S. M., Koo, D. C., et al. 2012, *ApJ*, **760**, 131
- Coil, A. L., Blanton, M. R., Burles, S. M., et al. 2011, *ApJ*, **741**, 8
- Coleman, G. D., Wu, C.-C., & Weedman, D. W. 1980, *ApJS*, **43**, 393
- Cooper, M. C., Newman, J. A., Coil, A. L., et al. 2007, *MNRAS*, **376**, 1445
- Coupon, J., Ilbert, O., Kilbinger, M., et al. 2009, *A&A*, **500**, 981
- Daddi, E., Dickinson, M., Morrison, G., et al. 2007, *ApJ*, **670**, 156
- Davé, R. 2008, *MNRAS*, **385**, 147
- Dressler, A. 1980, *ApJ*, **236**, 351
- Dressler, A., & Gunn, J. E. 1983, *ApJ*, **270**, 7
- Dunne, L., Ivison, R. J., Maddox, S., et al. 2009, *MNRAS*, **394**, 3
- Dutton, A. A., van den Bosch, F. C., & Dekel, A. 2010, *MNRAS*, **405**, 1690
- Elbaz, D., Daddi, E., Le Borgne, D., et al. 2007, *A&A*, **468**, 33

- Faber, S. M., Willmer, C. N. A., Wolf, C., et al. 2007, *ApJ*, **665**, 265
- Font, A. S., Bower, R. G., McCarthy, I. G., et al. 2008, *MNRAS*, **389**, 1619
- Gerke, B. F., Newman, J. A., Davis, M., et al. 2012, *ApJ*, **751**, 50
- Gerke, B. F., Newman, J. A., Faber, S. M., et al. 2007, *MNRAS*, **376**, 1425
- Giodini, S., Finoguenov, A., Pierini, D., et al. 2012, *A&A*, **538**, A104
- Gladders, M. D., & Yee, H. K. C. 2005, *ApJS*, **157**, 1
- Gómez, P. L., Nichol, R. C., Miller, C. J., et al. 2003, *ApJ*, **584**, 210
- Gunn, J. E., & Gott, J. R. I. 1972, *ApJ*, **176**, 1
- Guo, Q., White, S., Li, C., & Boylan-Kolchin, M. 2010, *MNRAS*, **404**, 1111
- Heinis, S., Buat, V., Béthermin, M., et al. 2014, *MNRAS*, **437**, 1268
- Hoaglin, D. C., Mosteller, F., & Tukey, J. W. (ed.) 1983, Wiley Series in Probability and Mathematical Statistics (New York: Wiley)
- Ilbert, O., Arnouts, S., McCracken, H. J., et al. 2006, *A&A*, **457**, 841
- Ilbert, O., Capak, P., Salvato, M., et al. 2009, *ApJ*, **690**, 1236
- Ilbert, O., Salvato, M., Le Floc'h, E., et al. 2010, *ApJ*, **709**, 644
- Jian, H.-Y., Lin, L., & Chiueh, T. 2012, *ApJ*, **754**, 26
- Jian, H.-Y., Lin, L., Chiueh, T., et al. 2013, *ApJ*, submitted (arXiv:1305.1891)
- Kaiser, N., Burgett, W., Chambers, K., et al. 2010, *Proc. SPIE*, **7733**, 12
- Kampczyk, P., Lilly, S. J., de Ravel, L., et al. 2013, *ApJ*, **762**, 43
- Kauffmann, G., Heckman, T. M., White, S. D. M., et al. 2003, *MNRAS*, **341**, 33
- Kauffmann, G., White, S. D. M., Heckman, T. M., et al. 2004, *MNRAS*, **353**, 713
- Kinney, A. L., Calzetti, D., Bohlin, R. C., et al. 1996, *ApJ*, **467**, 38
- Knobel, C., Lilly, S. J., Iovino, A., et al. 2009, *ApJ*, **697**, 1842
- Kovac, K., Lilly, S. J., Knobel, C., et al. 2013, *MNRAS*, submitted (arXiv:1307.4402)
- Koyama, Y., Smail, I., Kurk, J., et al. 2013, *MNRAS*, **434**, 423
- Kriek, M., van Dokkum, P. G., Labbé, I., et al. 2009, *ApJ*, **700**, 221
- Larson, R. B., Tinsley, B. M., & Caldwell, C. N. 1980, *ApJ*, **237**, 692
- Li, I. H., Glazebrook, K., Gilbank, D., et al. 2011, *MNRAS*, **411**, 1869
- Lilly, S. J., Le Fèvre, O., Renzini, A., et al. 2007, *ApJS*, **172**, 70
- Liu, H. B., Hsieh, B. C., Ho, P. T. P., Lin, L., & Yan, R. 2008, *ApJ*, **681**, 1046
- Lin, L., Cooper, M. C., Jian, H.-Y., et al. 2010, *ApJ*, **718**, 1158
- Lin, L., Dickinson, M., Jian, H. Y., et al. 2012, *ApJ*, **756**, 71
- Lin, L., Koo, D. C., Weiner, B. J., et al. 2007, *ApJL*, **660**, L51
- Lotz, J. M., Jonsson, P., Cox, T. J., & Primack, J. R. 2010, *MNRAS*, **404**, 590
- Magdis, G. E., Rigopoulou, D., Huang, J.-S., & Fazio, G. G. 2010, *MNRAS*, **401**, 1521
- Magnier, E. 2006, in The Advanced Maui Optical and Space Surveillance Technologies Conference, ed. S. Ryan (Kihei, HI: Maui Economic Board), **E50**
- Magnier, E. A., Schlafly, E., Finkbeiner, D., et al. 2013, *ApJS*, **205**, 20
- McGee, S. L., Balogh, M. L., Bower, R. G., Font, A. S., & McCarthy, I. G. 2009, *MNRAS*, **400**, 937
- McGee, S. L., Balogh, M. L., Wilman, D. J., et al. 2011, *MNRAS*, **413**, 996
- Metcalf, N., Farrow, D. J., Cole, S., et al. 2013, *MNRAS*, **435**, 1825
- Mihos, J. C., & Hernquist, L. 1994, *ApJL*, **431**, L9
- Mok, A., Balogh, M. L., McGee, S. L., et al. 2013, *MNRAS*, **431**, 1090
- Molino, A., Benítez, N., Moles, M., et al. 2013, arXiv:1306.4968
- Moore, B., Katz, N., Lake, G., Dressler, A., & Oemler, A. 1996, *Natur*, **379**, 613
- Mostek, N., Coil, A. L., Moustakas, J., Salim, S., & Weiner, B. J. 2012, *ApJ*, **746**, 124
- Moustakas, J., Coil, A. L., Aird, J., et al. 2013, *ApJ*, **767**, 50
- Muzzin, A., Wilson, G., Yee, H. K. C., et al. 2012, *ApJ*, **746**, 188
- Newman, J. A., Cooper, M. C., Davis, M., et al. 2013, *ApJS*, **208**, 5
- Noeske, K. G., Weiner, B. J., Faber, S. M., et al. 2007, *ApJL*, **660**, L43
- Onaka, P., Tonry, J. L., Isani, S., et al. 2008, *Proc. SPIE*, **7014**, 120
- Oppenheimer, B. D., & Davé, R. 2008, *MNRAS*, **387**, 577
- Pannella, M., Carilli, C. L., Daddi, E., et al. 2009, *ApJL*, **698**, L116
- Patel, S. G., Kelson, D. D., Holden, B. P., Franx, M., & Illingworth, G. D. 2011, *ApJ*, **735**, 53
- Patton, D. R., & Atfield, J. E. 2008, *ApJ*, **685**, 235
- Peng, Y.-j., Lilly, S. J., Kovač, K., et al. 2010, *ApJ*, **721**, 193
- Quadri, R. F., Williams, R. J., Franx, M., & Hildebrandt, H. 2012, *ApJ*, **744**, 88
- Quilis, V., Moore, B., & Bower, R. 2000, *Sci*, **288**, 1617
- Robotham, A., Phillipps, S., & de Propris, R. 2010, *MNRAS*, **403**, 1812
- Robotham, A., Wallace, C., Phillipps, S., & De Propris, R. 2006, *ApJ*, **652**, 1077
- Stubbs, C. W., Doherty, P., Cramer, C., et al. 2010, *ApJS*, **191**, 376
- Tonry, J. L., Stubbs, C. W., Kilic, M., et al. 2012, *ApJ*, **745**, 42
- Tonry, J. L., Stubbs, C. W., Lykke, K. R., et al. 2012, *ApJ*, **750**, 99
- Tran, K.-V. H., Papovich, C., Saintonge, A., et al. 2010, *ApJL*, **719**, L126
- Vulcani, B., Poggianti, B. M., Finn, R. A., et al. 2010, *ApJL*, **710**, L1
- Wetzel, A. R. 2011, *MNRAS*, **412**, 49
- Wetzel, A. R., Tinker, J. L., Conroy, C., & van den Bosch, F. C. 2013, *MNRAS*, **432**, 336
- Whitaker, K. E., van Dokkum, P. G., Brammer, G., & Franx, M. 2012, *ApJL*, **754**, L29
- White, S. D. M., & Frenk, C. S. 1991, *ApJ*, **379**, 52
- Wijesinghe, D. B., Hopkins, A. M., Brough, S., et al. 2012, *MNRAS*, **423**, 3679
- Willmer, C. N. A., Faber, S. M., Koo, D. C., et al. 2006, *ApJ*, **647**, 853
- York, D. G., Adelman, J., Anderson, J. E., Jr., et al. 2000, *AJ*, **120**, 1579
- Zeimann, G., Stanford, S. A., Brodwin, M., et al. 2013, *ApJ*, **779**, 137